# Interpenetration and deflection phenomena in collisions between supersonic, magnetized, tungsten plasma flows diagnosed using high resolution optical Thomson scattering

G. F. Swadling, S. V. Lebedev, A. J. Harvey-Thompson, W. Rozmus, G. Burdiak, L. Suttle, S. Patankar, R. A. Smith, M. Bennett, G. N. Hall, F. Suzuki-Vidal, S. Bland, and J. Yuan

Citation: Physics of Plasmas **22**, 072706 (2015); doi: 10.1063/1.4926579
View online: http://dx.doi.org/10.1063/1.4926579
View Table of Contents: http://scitation.aip.org/content/aip/journal/pop/22/7?ver=pdfcov
Published by the AIP Publishing



# Interpenetration and deflection phenomena in collisions between supersonic, magnetized, tungsten plasma flows diagnosed using high resolution optical Thomson scattering

G. F. Swadling,[1] S. V. Lebedev,[1] A. J. Harvey-Thompson,[2] W. Rozmus,[3] G. Burdiak,[1] L. Suttle,[1] S. Patankar,[1] R. A. Smith,[1] M. Bennett,[1] G. N. Hall,[1,a)] F. Suzuki-Vidal,[1] S. Bland,[1] and J. Yuan[4]
[1]*Blackett Laboratory, Imperial College, London SW7 2BW, United Kingdom*
[2]*Sandia National Laboratories, PO Box 5800, Albuquerque, New Mexico 87185-1193, USA*
[3]*Department of Physics, University of Alberta, Edmonton, Alberta T6G 2J1, Canada*
[4]*Key Laboratory of Pulsed Power, Institute of Fluid Physics, CAE, Mianyang 621900, China*

(Received 1 May 2015; accepted 19 June 2015; published online 14 July 2015)

An optical Thomson scattering diagnostic has been used to investigate collisions between supersonic, magnetized plasma flows, in particular the transition from collisionless to collisional interaction dynamics. These flows were produced using tungsten wire array z-pinches, driven by the 1.4 MA 240 ns Magpie generator at Imperial College London. Measurements of the collective-mode Thomson scattering ion-feature clearly indicate that the ablation flows are interpenetrating at 100 ns (after current start), and this interpenetration continues until at least 140 ns. The Thomson spectrum at 150 ns shows a clear change in the dynamics of the stream interactions, transitioning towards a collisional, shock-like interaction of the streams near the axis. The Thomson scattering data also provide indirect evidence of the presence of a significant toroidal magnetic field embedded in the "precursor" plasma near the axis of the array over the period 100–140 ns; these observations are in agreement with previous measurements [Swadling *et al.*, Phys. Rev. Lett. **113**, 035003 (2014)]. The Thomson scattering measurements at 150 ns suggest that this magnetic field must collapse at around the time the dense precursor column begins to form. © *2015 AIP Publishing LLC*.
[http://dx.doi.org/10.1063/1.4926579]

## I. INTRODUCTION

The interaction dynamics of colliding supersonic plasma flows is of interest to researchers working in a wide range of fields. Such collisions are ubiquitous in astrophysics and play an important role in many high energy density physics and inertial confinement fusion (ICF) experiments. Various research groups have carried out investigations of these interactions over a wide range of plasma parameters, using a variety of different acceleration mechanisms and diagnostic techniques.

Collisions between streams of plasma produced from laser-ablated targets have been studied extensively at facilities, such as LULI at École Polytechnique,[1] GXII at the Institute of Laser Engineering, Osaka,[2] the OMEGA Laser Facility at Rochester University,[3–6] and most recently on the National Ignition Facility at Lawrence Livermore National Laboratory.[7] These experiments were designed to investigate the interpenetration and interactions of pairs of colliding flows; the aims were to gain a better understanding of the structures formed in ICF hohlraums, to study the formation of collisionless shocks and to study the self-organized and enhanced magnetic and electric field structures which can be formed due to the various plasma instabilities (e.g., Weibel[8]).

Taking a different approach, recent experiments conducted on the Plasma Liner Experiment at Los Alamos National Laboratory (LANL) have studied meter-length-scale interactions between plasma flows accelerated using pulsed-power driven railguns.[9] These experiments have investigated both oblique shock formation[10,11] between radially converging streams and flow interpenetration and stagnation in the transitional phase between collisionless and fully collisional behavior.[12]

In this paper, we discuss the results of recent experiments studying the interactions of supersonic, magnetized plasma flows produced using the Magpie[13] pulsed power generator (1.4 MA, 240 ns) at Imperial College. Previously, this machine has been used to drive experiments investigating the interactions of dense, supersonic plasma jets produced from conical wire arrays, both with static plasma clouds and with cross-winds,[14,15] and the collisions and interactions of jets launched from radial foils with ambient media.[16,17] More recently, experiments have been designed to study the formation of oblique shocks[18] and to investigate the interpenetration of the radially convergent plasma ablation flows produced by wire array z-pinches.[19,20] These experiments have been diagnosed using a combination of laser interferometric imaging and Thomson scattering (TS).[21]

The plasma parameters of the flows (velocity, density and temperature) produced in Magpie experiments tend to fall between those produced in laser driven experiments and

[a)]Current address: Lawrence Livermore National Laboratory, P.O. Box 808, Livermore, California 94551, USA.

 

those produced in the railgun driven experiments. What is unique about the Magpie experiments is that the magnetic (Lorentz force) mechanism which accelerates the flows also embeds a frozen magnetic field into them. This field, which is advected with the ablation flows, can go on to have dynamically significant effects on the interactions of the colliding streams. The interactions of magnetized flows are of great interest to the community,[22,23] however introducing external magnetization to laser driven flows is difficult[24] and the parameters of railgun driven outflows mean that the magnetic diffusion time is substantially smaller than the experimental timescale, such that the magnetic field induced in the plasma during acceleration is not advected with the flow.[10] The process of magnetic flux advection in wire array ablation flows has been measured directly using B-dot magnetic field probes[25,26] in imploding wire arrays, and using Faraday rotation imaging in exploding wire array experiments.[21] Furthermore, recent Thomson scattering measurements have provided indirect evidence that the ablation streams in wire arrays are deflected by a toroidal magnetic field which is advected to and accumulated around the array axis.[20] Results from experiments investigating the interactions of outflows from exploding wire arrays with conducting obstacles suggest that the magnetization of these flows may make it possible to study phenomena, such as magnetized shocks and magnetic reconnection.[27]

The work presented in this paper is an extension of previous investigations of the collision of ablation streams on the axes of tungsten wire arrays.[19,20] Tungsten wire arrays are of particular interest because it has long been thought that the ablation streams should interpenetrate across the array axis at early times.[28–31] An improved Thomson scattering diagnostic, with increased spatial and spectral resolution, has been used to make measurements over a broad range of experimental times (100 ns–160 ns from current start). These measurements allow us to observe the transition from almost fully collisionless interactions to the point at which collisional dynamics begin to dominate.

## II. EXPERIMENTAL SETUP

The experiments presented in this paper were carried out using 20 mm long, 16 mm Ø cylindrical wire arrays consisting of eight evenly distributed 18 $\mu$m Ø tungsten wires. The arrays were mounted in the generator using a specially designed electrode hardware configuration which places the wire array on its side so that its axis lies perpendicular to the axis of the coaxial pulsed-power drive electrodes.[32] This arrangement does introduce some small current drive asymmetries; this disadvantage is however easily overcome by the advantage of the diagnostic access that this layout allows. Mounting the array in this manner provides an unobscured end-on view through the wire array interior, easing interferometry access, and allowing us to use a much improved Thomson scattering geometry. Fig. 1(a) shows a schematic diagram of this arrangement.

A two-color, two-time, end-on laser interferometric imaging diagnostic was used to measure spatial variations in the axially-integrated electron density ($\int n_e dz$) of the plasma,

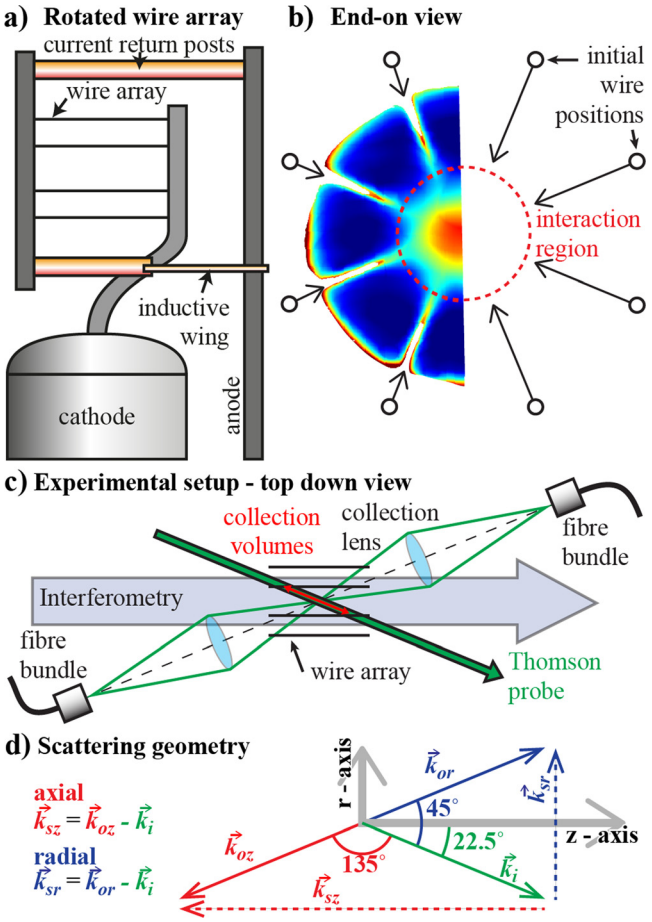


FIG. 1. Experimental setup. (a) Side on view of experimental hardware, showing rotated array configuration.[32] (b) Diagram of end-on view. Left, example $n_e$ map extracted from interferogram, right schematic of flow vectors. (c) Top-down view of the Thomson scattering alignment. (d) Vector scattering geometry diagram.

and an optical TS diagnostic was used to measure the ion-component of the TS spectrum in order to infer bulk ion velocities and temperatures.[21] These diagnostics were complimented by a 12-frame, time resolved (5 ns) optical emission imaging diagnostic, which was fielded in order to produce a single-shot overview of the array dynamics.

The interferometer used a Mach-Zehnder layout, powered by 2nd (532 nm) and 3rd (355 nm) harmonic beams from a commercial Nd:YAG pulsed laser system (EKSPLA SL312P). The overall setup was similar to the layout shown in Ref. 18, except that the rotated array configuration used in these experiments removed the need for the cathode mounted mirror, allowing laser probing to be carried out at significantly later times.[32] These probe beams had pulse durations of ~500 ps, diameters of ~2 cm, and a total energy per pulse of ~10 mJ. Interferograms were captured using Canon DSLR cameras. The shutters of these cameras were held open for the entire duration of the experiment; a combination of spatial and laser-line spectral filtering was used to ensure that the optical energy delivered to the CCD by the probe beam was significantly greater than that delivered by the time-integrated self-emission from the experiment. The time resolution of the recorded image was set simply by the pulse-duration of the laser. The end-on orientation of the

interferometer produced the view shown in Fig. 1(b); the orientation of the probe beam is also indicated in the schematic in Fig. 1(c). The interferograms were analyzed using the fringe interpolation techniques described in our previous publications,[18,19,21] resulting in maps of the variation of $\int n_e dz$ across the radial-azimuthal $(r, \phi)$ plane of the array.

The TS diagnostic used a scattering geometry which produces simultaneous, independent measurements of the axial ($z$) and radial ($r$) components of the ion velocity distribution of the plasma. This geometry has been used successfully in previous experiments to diagnose ablation stream interpenetration and deflection in tungsten wire arrays[20] and is discussed in detail in Ref. 21. Making simultaneous, independent measurements of the axial and radial components of the plasma velocity distribution significantly simplifies the analysis and interpretation of the TS data.

Diagrams of the scattering geometry used in these experiments are shown in Figs. 1(c) and 1(d). The wave-vector of the incoming TS probe beam ($\vec{k}_i$) is aligned through the center of the wire array at an angle 22.5° from the axis. Light scattered by the plasma is collected from a pair of counter-facing collection-vectors ($\vec{k}_{or}$ and $\vec{k}_{oz}$) which lie in the same plane, on the line 22.5° the other side of the axis from $\vec{k}_i$. The scattered spectrum recorded from any given collection-vector is sensitive only to the components of the velocity distribution which lie parallel to the specific scattering wave-vector, $\vec{k}_s \equiv \vec{k}_o - \vec{k}_i$. From Fig. 1(d), we can see that the pair of $\vec{k}_s$ that result from the geometry used in this experiment lie parallel to the radial ($\vec{k}_{sr}$, red) and axial ($\vec{k}_{sz}$, blue) coordinate axes of the array. The magnitudes of $\vec{k}_{sr}$ and $\vec{k}_{sz}$ are different; this has an effect on the measured spectra, as the Doppler shift associated with any given scattering event is given $\delta\omega_D = \vec{k}_s \cdot \vec{v}$, where $\vec{v}$ is the velocity of the scattering charge. In these experiments, $|\vec{k}_{sz}|/|\vec{k}_{sr}| = 2.4$, and thus, for an isotropic ion velocity distribution, the TS spectrum recorded by the axially sensitive channel will be ×2.4 broader than that recorded by the radially sensitive channel. The total optical power scattered along $\vec{k}_{or}$ and $\vec{k}_{oz}$ should be approximately equal, however for $\vec{k}_{oz}$, this power is spread over a broader spectral range, so the recorded spectrum will also be less intense.

In our previous experiments, the scattered spectrum was collected using a pair of linear fiber arrays, each consisting of $7 \times 200\,\mu$m Ø fibers.[20,33,34] For the experiments presented in this paper, these have been replaced with a pair of $14 \times 100\,\mu$m Ø fiber arrays. There are two advantages to using these higher density fiber arrays, firstly the number of spatial positions from which the spectra may be collected is doubled and secondly, the decreased fiber diameter means the effective source size at the spectrometer input slit is narrower, resulting in better spectral resolution. The best resolution achieved on the TS diagnostic using the 200 $\mu$m Ø fibers was 0.5 Å; with the new fibers, we have achieved 0.35 Å. The main disadvantage of using the new, finer fibers is that the cross-sectional area over which scattered light is collected is reduced. In some cases, when measurements were made at early times and the electron density of the plasma was relatively low, the scattered power was substantially reduced, leading to a reduction in the signal-to-noise ratio of the measured spectra. Further specific details of the TS diagnostic setup, including details of the optics, spectrometer, and camera system used may be found in Ref. 21.

## III. OVERVIEW OF ABLATION DYNAMICS IN TUNGSTEN WIRE ARRAYS

The data presented in this paper originates from a series of five nominally identical experiments; measurements of the Magpie drive-current waveforms are presented in Fig. 2 in order to illustrate the high degree of shot-to-shot reproducibility achieved. The plot includes the current wave form measured in the experiment reported in Ref. 20. The close similarity of the current drives in all these experiments means that straightforward comparisons may be made between measurements taken over a wide range of experimental times across all five of these shots.

The timings of the main measurements made during the experimental campaign are marked in Fig. 2 by a series of vertical lines; all timings are given with respect to $t = 0$ at current start. The 532 nm interferometry timings are marked by green lines, 355 nm interferometry by blue lines, and TS measurement times by red lines. The interferograms, captured at the times indicated in Fig. 2, have been analyzed in order to produce a time-series of end-on maps of $L^{-1}\int n_e dz$, the areal electron density averaged over the length of the array ($L = 20$ mm). The series of images, presented in Fig. 4, provides an overview of the evolution of the ablation stream interaction dynamics up until approximately the time at which the dense precursor column is formed.[31] A time series of side-on optical self-emission images, presented in Fig. 3, provide a further overview of the dynamics and confirm that dense precursor formation starts at approximately 155–160 ns, indicated by a slight darkening on the axis of the array at around this time.

Starting with the earliest data presented in Fig. 4, at 77 ns, the electron density distribution around the axis appears broad and smooth. Sharp, well-focused ablation streams are seen extending from each of the wire cores, however these

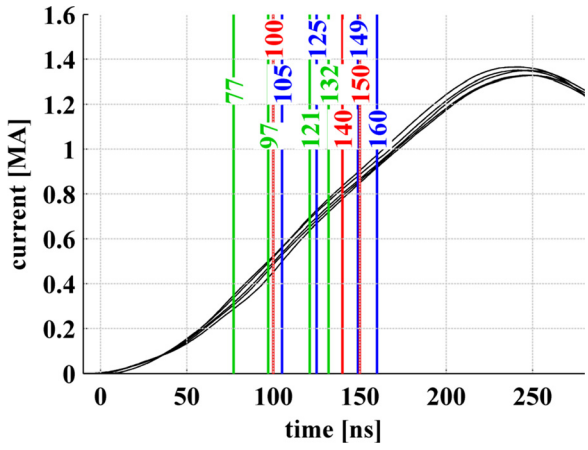


FIG. 2. Plots of current vs. time for the five shots for which the data presented in this paper were collected. Current curves are plotted as black lines, diagnostic timings are plotted as green and blue vertical lines for 532 and 355 nm interferometry, respectively, and red vertical lines for TS measurements. The plot demonstrates the high degree of shot-to-shot current drive reproducibility achieved in this series of experiments.

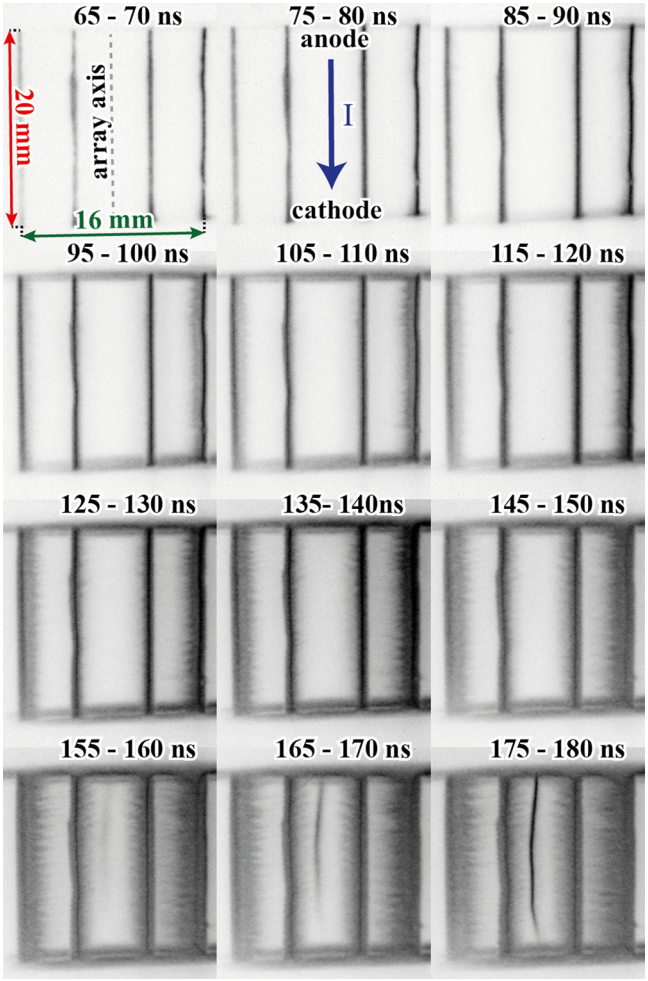


FIG. 3. Side-on time gated optical self-emission images of wire array. Temporal resolution ~5 ns. The 155 ns frame shows evidence for the early stages of dense precursor column collapse.

do not extend very far towards the axis, perhaps only ~2–3 mm; closer to the axis, there is little azimuthal modulation of $L^{-1}\int n_e dz$. Later in time, at 97 ns, the radius of the broad, smooth distribution of $L^{-1}\int n_e dz$ about the axis appears to have perhaps slightly expanded. As time goes on, more and more plasma arrives from the wire cores and the peak electron density on axis therefore gradually increases. The radius of the smooth distribution of plasma about the axis begins to contract at around 105–120 ns and from 125 to 160 ns, the rate of this radial contraction appears to increase. Focused ablation streams are seen to extend further and further towards the array axis, and in the final two images, as the time approaches 160 ns, precursor column collapse is observed;[28] the timing of this collapse correlates well with the expected peak in emission associated with precursor formation in tungsten arrays, at around 160 ns (Ref. 31) (radiative flux was not measured in these experiments), and also with the appearance of a narrow column of strongly emitting plasma in the optical self-emission images in Fig. 3.

These qualitative assessments are backed up by a more quantitative analysis. Examples of three different normalized profiles of electron density measured along the diameter of the array are also presented in Fig. 4. These profiles were taken through the array axis along the lines indicated by the green triangles in the corresponding $L^{-1}\int n_e dz$ plots. The profiles illustrate the changing "width" of the distribution of plasma about the axis; the widths of these distributions are clearly decreasing with time. In Fig. 5, the full-width half-maxima (FWHM) measured from all the $L^{-1}\int n_e dz$ maps in Fig. 4 are plotted against time, alongside the electron density measured at the array axis. The width of the distribution initially remains reasonably constant, at ~4–4.5 mm, until around 120–130 ns when it undergoes a rapid collapse towards a radius ×4 smaller at 160 ns. It should be noted that no peak electron density on axis could be measured at 160 ns, as the probe laser was obscured by the dense plasma. The value of the FWHM for this time was therefore calculated using the peak electron density from the previous measurement as the normalization factor. As a result, the FWHM should be treated as a highly conservative upper bound. It is very likely, considering the rate of increase in density on axis seen between the previous two measurements and continuing increase in drive current, that the radius of the distribution of plasma is substantially smaller at this time; a simple linear extrapolation of the $n_e$ on axis using the data points at 132 and 149 ns in Fig. 5 suggests that the true FWHM is <0.7 mm, lying within the central, obscured region of the 160 ns $L^{-1}\int n_e dz$ map.

The evolution of the precursor plasma column seen in the end-on interferometry data in Fig. 4 agrees qualitatively with previous descriptions of the behavior of the early time, broad, pre-collapse precursor,[19,28,31] but adds new, detailed, quantitative information about the evolution of the electron density during this period. The key observation is the presence of a broad, smooth distribution of plasma near the axis of the array, fed by distinct, sharply focused ablation streams that originate from each individual wire core. This broad distribution lacks the azimuthal modulation which might be expected to be imprinted into it due to the discrete nature of the ablation streams that feed into it. The radius of this smoothed "interaction" region appears to remain roughly constant, before undergoing a rapid collapse to high density, starting at around 120 ns.

## IV. THOMSON SCATTERING MEASUREMENTS

Thomson scattering measurements were taken at 100 ns, 140 ns, and 150 ns using the new 14-fiber array described in Section II; these timing are marked by red vertical lines on the diagram in Fig. 2 and the corresponding raw TS spectrograms are presented in Figs. 6(a)–6(c), respectively. In these images, the vertical axis corresponds to the direction along the spectrometer input slit, whilst the horizontal axis corresponds to the direction of spectral dispersion. The horizontal bands across the images each correspond to the spectrum recorded from one individual fiber. The top 14 bands correspond to the fibers recording scattering along the radially sensitive collection vector ($\hat{k}_{or}$), while the bottom 13 correspond to fibers collecting from the axially sensitive collection vector ($\hat{k}_{oz}$) (there is insufficient space to fit all 14 axial fiber signals onto the iCCD). In order to aid reference, the radial and azimuthal positions of the 14 volumes from which scattered light was collected are indicated on the

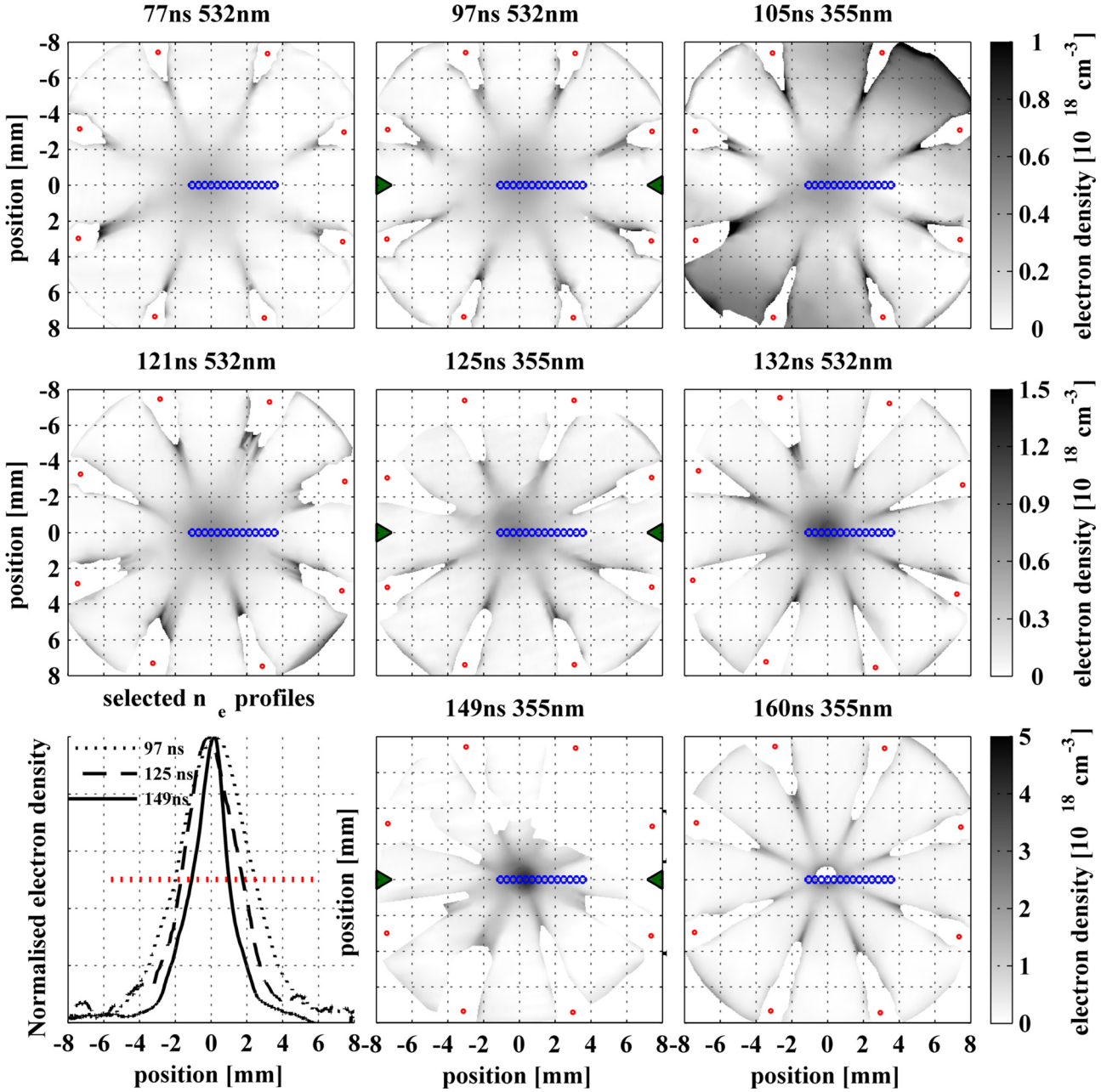


FIG. 4. A series of electron density plots showing the evolution of the electron density in the interior of an eight wire tungsten array over the period 77 ns–160 ns. Initial wire positions are indicated by red spots. Thomson scattering volumes are indicated by blue circles. Bottom left corner shows a selection of three normalized electron density profiles taken through the array axis. Profile positions are indicated by green arrows on relevant plots. FWHM (taken along red dotted line) and density on axis extracted from these plots are presented in Fig. 5.

electron density plots in Figs. 4 and 6 by small blue circles. A cursory inspection of the three TS spectrograms reveals a wide variation in structure; however, the individual spectral features were shown to be reproducible between measurements carried out at similar times. The variation in structure is indicative of the changing dynamics of the collisions between plasma streams over the timescale of the three measurements.

In Sections IV A–IV C, we present analysis and interpretation of the TS spectra and discuss the types of interaction dynamics with which they are consistent. As a starting point, we take the measurement at 140 ns, which is most similar to the spectral structure seen in previous experiments.[20] We will then look at the differences seen in the spectrum at 100 ns and 150 ns. These discussions are quite general, and errors have not been specified for each individual measurement. Errors in the determination of the radial ($v_r$) and axial ($v_z$) velocities are approximately $\pm 1 \times 10^4\,\mathrm{ms}^{-1}$ and $\pm 5 \times 10^3\,\mathrm{ms}^{-1}$, respectively. Errors in ion-temperature are typically larger, on the order of 20% of the quoted value. This uncertainty stems from the low sensitivity of the spectral width to the ion temperature, and also uncertainties in the exact form of the spectrometer function. The temperatures have all been assessed using the same method, so these errors should be systematic, and should therefore not impact any observed trends.

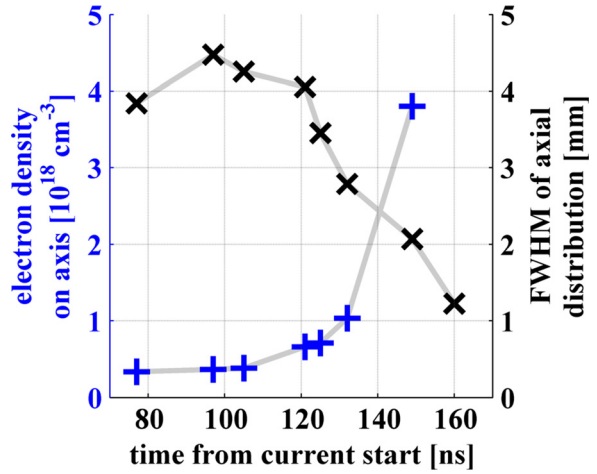


FIG. 5. Plots of variation with time of measured electron density on axis (blue) and the width of the electron distribution (black) near the axis. These profiles were extracted from the end-on $\frac{1}{L}\int n_e dz$ distribution maps in Fig. 4.

### A. 140 ns—Interpenetration, thermalization, and deflection

The structure of the TS spectrum measured at 140 ns is consistent with long-range collisional interactions between the radially converging ablation streams. Previously, the authors have analyzed TS data captured in a similar experiment at 120 ns;[20] the structure for the TS spectrum measured at 140 ns is qualitatively very similar to the structure seen in that experiment.

The upper half of the 140 ns spectrogram (Fig. 6(b)) contains the spectra recorded from fibers along the radially-sensitive scattering vector. Qualitatively, at large radius, the spectra appear to consist of a narrow, red-shifted spectral peak superposed over a broader, un-shifted spectral distribution. Approaching the axis, this peak gradually broadens and its red-shift decreases. The narrow, red-shifted peak corresponds to the incoming ablation streams. These data indicate that the incoming streams lose radial velocity and their ion temperatures increase as they approach the array axis.

The lower half of the spectrogram contains the spectra recorded along the axially-sensitive scattering vector. As in the case of the radially-sensitive spectra, the spectra recorded from the scattering volumes closer to the axis appear broader, consistent with an increasing ion temperature. The axial spectra close to the axis are characterized by a significant blue-shift, indicating that the plasma has acquired a significant axial velocity component as it has approached the array axis. As observed in previous experiments,[20] this axial velocity component is directed towards the anode-end of the array, and the ion trajectory is therefore consistent with the deflection of the flows due to the presence of a magnetic field accumulated about the axis of the array (see Ref. 20 for further discussion).

It appears that the collisional scale length for the ablation stream interactions is long enough to allow significant interpenetration of the flows whilst also mediating the thermalization of the directed kinetic energy of the streams over the scale length of the region over which the measurements were made (~3–4 mm). At the same time, the

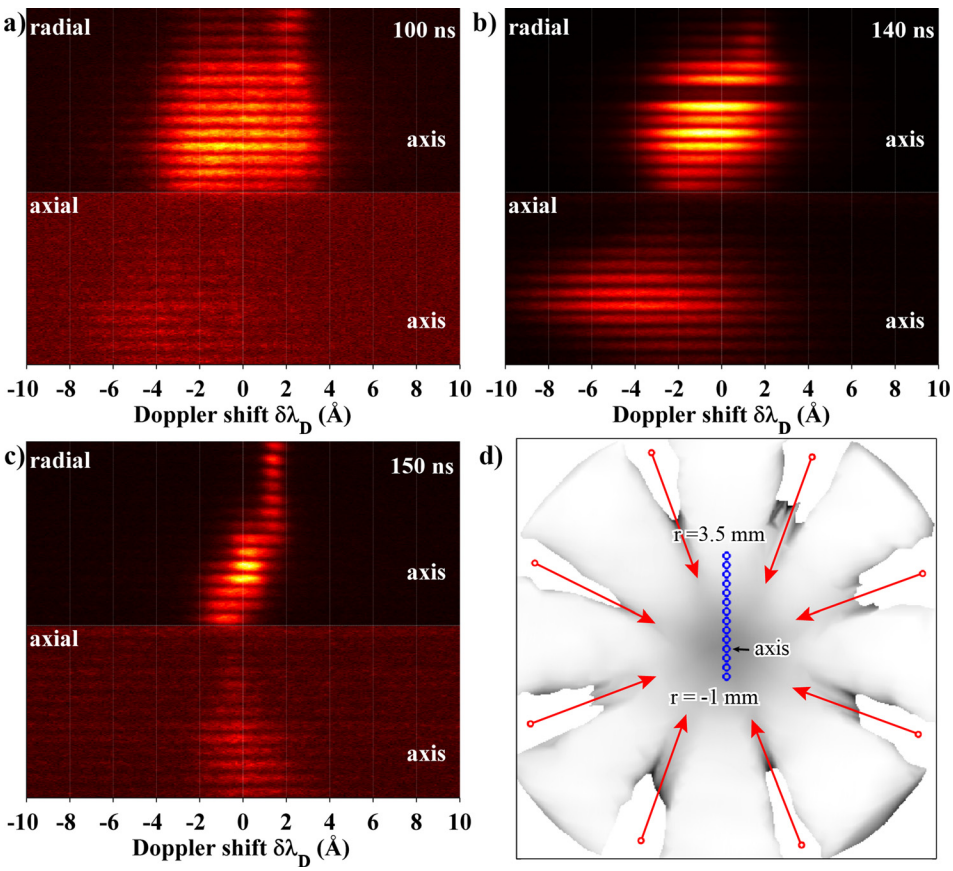


FIG. 6. Raw Thomson scattering spectra, as recorded by the spectrometer. (a)–(c) Spectra recorded at 100, 140, and 150 ns, respectively. Vertical axis corresponds to direction along spectrometer input slit, horizontal to direction of spectral dispersion. Each horizontal band corresponds to the spectrum from a single fiber. The upper 14 fibers correspond to radially sensitive scattering vector, the lower 13 to axially sensitive scattering vector. Fibers collect from scattering volumes indicated in diagram (d). Volumes in diagram and spectrograms run vertically in the same direction.

interpenetrating streams appear to be being deflected by a static, toroidal magnetic field which has built up around the array axis. This field is most likely formed through the accretion of magnetic field advected towards the axis by the incoming ablation streams and stagnated with the magnetized, electron component of the plasma[20] (this will be discussed in greater detail later).

A quantitative analysis of the 140 ns TS spectra is presented in Fig. 7. This analysis was carried out using the simultaneous fit method described in our previous publications.[20,21] The fits to the experimental data were calculated using the multiple-ion-species, non-relativistic, Maxwellian spectral density function[35] ($S(\omega,k)$)

$$S(\omega,k)=\frac{2\pi}{k}\left[\left|1-\frac{\chi_e}{\epsilon}\right|^2 f_{e0}\left(\frac{\omega}{k}\right)+\sum_j \frac{\bar{Z}_j^2 n_j}{n_e}\left|\frac{\chi_e}{\epsilon}\right|^2 f_{i0}\left(\frac{\omega}{k}\right)\right]$$
$$\epsilon=1+\chi_e+\sum_j \chi_j, \qquad n_e=\sum_j n_j \bar{Z}_j. \tag{1}$$

In this equation, $f_{eo}$ and $f_{jo}$ are the Maxwellian velocity distributions, $\chi_e$ and $\chi_j$ are the electric susceptibilities, and $n_j$ is the density of the $j$th ion population (subscript $j$) and electrons (subscript $e$). Parameters $\omega$ and $k$ are the frequency and wavenumber shifts required to produce the observed scattering. The equations used to calculate the susceptibilities are written:[35]

$$\chi_e=\frac{-1\alpha^2}{2}Z'\left(\frac{\omega}{kv_{Te}}\right),\ \chi_j=\frac{-1\alpha^2}{2}\frac{\bar{Z}T_e}{T_j}Z'\left(\frac{\omega}{kv_{Ti}}\right)$$
$$Z'(\zeta)=\frac{1}{\sqrt{\pi}}\int_{\infty}^{\infty}\frac{e^{-t^2}dt}{t-\zeta},$$
$$v_{Te/i}=\sqrt{\frac{2k_BT_{e/i}}{m_{e/i}}},\ \alpha=\frac{1}{k\lambda_{De}}, \tag{2}$$

where $Z'(\zeta)$ is the plasma dispersion function and $v_{Te/j}$ is the characteristic thermal velocity of the electrons/$j$th ion population.

Fits for the radial and axial scattering vectors were calculated simultaneously for each scattering volume. The plasma in each volume was modeled as consisting of two counter-propagating, interpenetrating ion populations (labeled $j=1$, 2) and a single electron population. Each ion population was described by its own set of independent parameters, ion density ($n_j$), ion temperature ($T_j$), average ionization ($\bar{Z}_j$), axial ($v_{zj}$), and radial velocities ($v_{rj}$). The electron thermal velocity was assumed to be much larger than the directed flow velocity of the plasma, and the electron-electron equilibration time was assumed to be much faster than the dynamic time of the experiment, such that the electrons in each scattering volume could be modeled as a single local population with a single density ($n_e=\sum_j n_j\bar{Z}_j$), temperature ($T_e$), and bulk velocity ($\boldsymbol{v_e}=(1/n_e)\sum_j \boldsymbol{v_j} n_j \bar{Z}_j$).

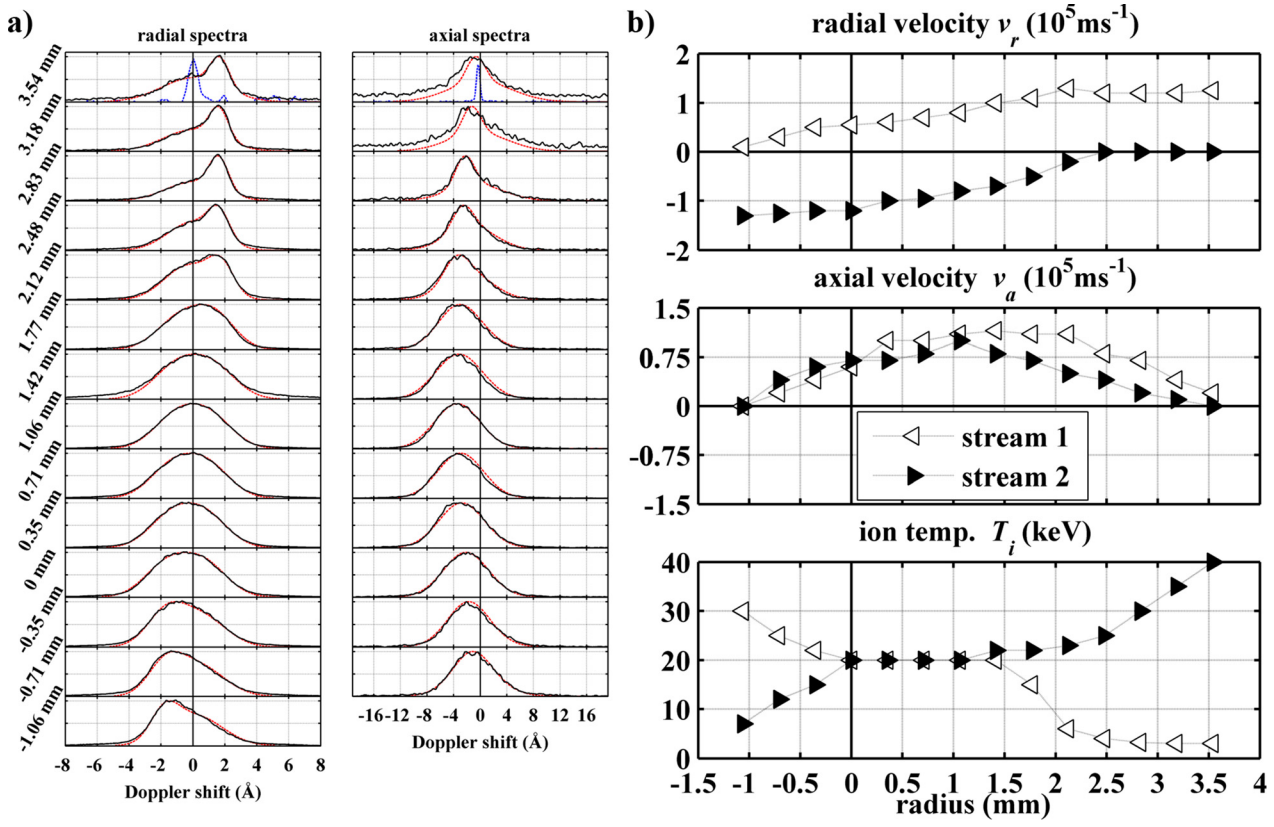


FIG. 7. Thomson scattering measurements at 140 ns. (a) Spectral profiles corresponding to each fiber. In black, spectral profiles extracted from spectrogram Fig. 6(b). In red, two-population spectral fits to data. In blue, pre-shot calibration of the un-shifted probe beam spectrum. (b) Plots of radial variation of various fitting parameters. Triangles indicate the radial direction of propagation of each ion-population.

The differences in the forms of the spectral profiles of the axial and radial fits come down to the differences in the scattering geometry (this modifies the magnitude of the scattering vector, $|\vec{k}_s|$, and therefore the Thomson scattering $\alpha$ parameter[35]) and to the differences in the magnitudes of the two velocity components $v_{rj}$ and $v_{zj}$. All other plasma parameters ($\bar{Z}_j$, $T_j$, $T_e$, $n_e$) are constrained to be shared between each pair of fits.

Spectral profiles corresponding to each fiber were extracted from the raw spectrogram (Fig. 6(b)) by summing over the spatial width of each signal. These profiles are plotted as black lines in Fig. 7(a). Normalized spectral fits are plotted as red lines and show excellent agreement with the data. The un-shifted laser-line is plotted in blue; this is used to calibrate both the central wavelength of the probe and the spectral response of the spectrometer. The variation with radius of the various plasma parameters used to produce these fits is plotted in Fig. 7(b).

The trends in the fitting parameters are similar to those seen in previous experiments;[20] the plasma flows are observed to initially approach the axis with a radial velocity of $\sim 1.2 \times 10^5\,\mathrm{ms}^{-1}$, a temperature of $\sim 2\,\mathrm{keV}$, and negligible axial velocity. As the flows approach the array axis, their radial velocities decrease and their axial velocities and temperatures increase. The axial velocities of the two flows peak on axis at $\sim 1.1 \times 10^5\,\mathrm{ms}^{-1}$; at this position, the ion temperature is $\sim 20\,\mathrm{keV}$, and radial velocity is only $\sim 7 \times 10^4\,\mathrm{ms}^{-1}$. On the far side of the axis, the temperature of ions continues to increase as both the axial and radial components of the ion velocity decrease. These observations are consistent with the long-scale-length thermalization of the directed kinetic energy of the flows as they interpenetrate through one another. The flows eventually lose all directed kinetic energy, reaching a peak ion temperature on the far side of the axis of $\sim 40\,\mathrm{keV}$.

The distribution of the fitting parameters in Fig. 7(b) is not symmetric about $r = 0$. The "dynamic axis" of the array instead appears to be shifted to one side by $\sim 0.5$–$1\,\mathrm{mm}$. There are a number of potential explanations for this. The fiber which collects light from the $r = 0$ scattering volume is aligned to light scattered from a pin which is placed at the axis of the array. There is likely to be an error associated with the exact placement of this pin, leading to a small ($\sim 0.5\,\mathrm{mm}$) offset in the radial positions of the scattering volumes. This does not affect the quoted inter-volume separations, as these are constrained by the probe laser and collection fiber geometry. Another possibility is that this displacement was caused by a small current drive asymmetry, which led the experiment to be driven slightly more on one side than the other. This asymmetry should have minimal impact on the interpretation of the results, as the analysis presented here is independent of spatial position.

The radial distribution of the fitting parameters is slightly modified from that seen in our previous experiment; in the region near the axis of the array, the spatial variation of the ion temperature distribution appears flattened; previously,[20] in a measurement at 120 ns, the ion temperature was observed to vary linearly across this region. Whilst the previous measurement had a lower spatial resolution, it seems unlikely that this effect was missed in the analysis; instead it seems plausible that the increasing density of the plasma on axis is driving a change in the plasma dynamics. Increased conduction of the ion's thermal energy might explain the observed spatial equilibration of the temperature profile. Ion-electron thermal equilibration is expected to become a significant effect at around this time, as evidenced by the observation of precursor column collapse at $\sim 160\,\mathrm{ns}$ in previous Magpie experiments[28,31,36] and in the optical self-emission images in Fig. 3. Although there is no interferogram at the exact time of this TS measurement, the progression of the electron density maps in Fig. 4, combined with the evidence from the images in Fig. 3, suggests that this measurement was made just prior to the start of the precursor collapse process. Further, more detailed measurements may be required to understand the details of this dynamic shift, in particular, it would be useful to have simultaneous measurements of both the electron temperature (through measurements of the Thomson scattering electron-feature) and of the radiative power (using, for example, a diamond photo-conducting detector array).

At this time, the axial velocity of the ions at the array axis actually exceeds the radial velocity by a significant factor. This suggests that the magnetic field has become more dynamically significant at this time, compare to our previous measurement at 120 ns.[20] This effect is discussed in greater detail in Section V B.

### B. Thomson spectrum at 100 ns

The TS spectrogram measured at 100 ns (Fig. 6(a)) immediately appears quite different from the spectrum seen at 140 ns. Qualitatively, the flows appear to be interacting in a much weaker manner, which is consistent with the reduced collisionality that would be expected given the lower density of the plasma at this time. As with the spectra at 140 ns, at large radius, the radially-sensitive spectra are dominated by a narrow, red-shifted spectral peak. This peak corresponds to the inwardly moving ablation stream. Nearer the axis, the spectral distribution becomes much broader, however the shapes of the spectral profiles suggest it is unlikely that this broadening is due to significant collisional thermalization of the ablation streams. The spectra have a broad, flattened, steep sided shape which appears to be formed by the superposition of scattering from many relatively cooler, interpenetrating streams passing through one another. This interpretation is further supported by the axially sensitive spectra, which are consistently significantly narrower than the corresponding radial spectra (even taking into account the ratio $|\vec{k}_{sz}|/|\vec{k}_{sr}| = 2.4$, as discussed in Section II).

A quantitative analysis of these spectra is presented in Fig. 8. The approach used to analyze these data is slightly different to the method used to model the spectra recorded at 140 ns. This is because the spectral profiles seen in the data at 100 ns are more complicated and cannot all be properly fitted using just two ion populations. Fig. 8(a) shows plots of the spectral profiles extracted from the spectrogram (Fig. 6(a)) for each of the 14 scattering volumes. The spectral

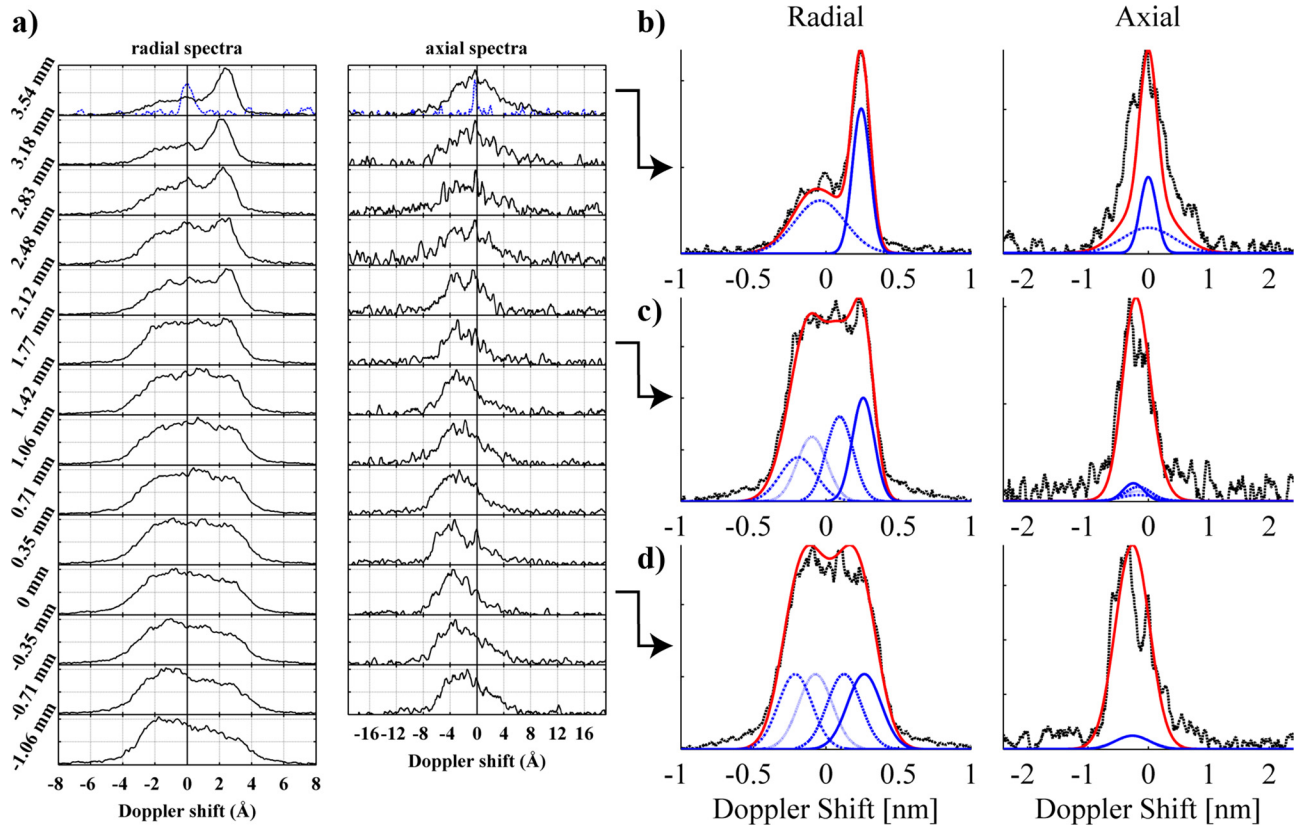


FIG. 8. Thomson scattering data analysis for measurement at 100 ns. (a) Individual spectra extracted from the spectrogram recorded at 100 ns (see Fig. 6). The black lines are the recorded Thomson scattering spectra, the blue line shows the un-scattered laser line used for calibration. (b)–(d) Three example fitting of this data. The arrows indicate the pairs of spectra which have been fitted. In black, measured spectrum; in red, spectral fit; in blue, individual ion population components of the each fit.

profiles are plotted using solid, black lines, while the spectrum of the un-shifted laser-line is again plotted in blue. The spectra from the radially sensitive fibers are shown in the left column, and the corresponding axially sensitive spectra are shown in the right column. Figs. 8(b)–8(d) show fitted spectra for three representative radial positions (positions indicated by arrows from Fig. 8(a)). In these plots, the raw data are plotted using dotted black lines, while the fits are shown by solid red lines. Spectra corresponding to the individual components of each fit are also shown, plotted with blue lines.

The first fit, Fig. 8(b), comes from the scattering volume which lies at the greatest radius ($r = \sim 3.5$ mm). Comparing with Fig. 4, we see that at $\sim$100 ns, this volume corresponds to a region just outside of the azimuthally smoothed "interaction-region." This volume is modeled with two ion populations. The radial spectrum has a narrow, tall spectral feature which corresponds to the incoming streams. This feature was fitted using a population with a velocity of $1.8 \times 10^5\,\mathrm{ms}^{-1}$ and an ion temperature of 3 keV to match the observed red-shift and broadening. The remaining spectrum appears to consist of a higher-temperature background plasma, modeled in the fit with a population with radial velocity of $-0.3 \times 10^5\,\mathrm{ms}^{-1}$ (i.e., away from the axis) and a temperature of 30 keV. This population likely corresponds to plasma that has already passed through the axis. The lack of any shift in the axial fit at this position indicates negligible axial velocity. The width of the fitted spectrum does not match the axial data as well as it does the radial data—this may be due to enhanced perpendicular diffusion of the stream's velocity distribution, but may also be influenced simply by the noise in the measurement—the axial spectra suffered from a significantly reduced signal to noise ratio at this early time. This was due to a combination of the low electron density of the plasma, which led to a reduced intensity of scattered light, and the difference in magnitude between the two scattering wave vectors, which meant the scattered power was spread over a larger spectral range for the axial measurements.

Plot Fig. 8(d) corresponds to the spectrum recorded from the scattering volume at the array axis. In this case, it was not possible to fit the spectra using a simple pair of ion populations; instead a more complicated model was found to be necessary. A diagram of the geometry for this scattering volume is shown in Fig. 9; it is assumed due to the cylindrical symmetry that the streams of plasma launched from each wire core have undergone the same collisional interactions and field deflections as they approached the axis. This implies that at the axis, each population should share the same temperatures ($T_i$, $T_e$), density ($n_i$), average ionization ($\bar{Z}_i$), and velocity magnitude $|\boldsymbol{v}|$. From the point of view of the TS diagnostic, the only difference between these flows should be the components of their velocities which lie parallel to the radial scattering vector ($\mathbf{v} \cdot \hat{\boldsymbol{k}}_{sr}$). Due to the alignment of the wires and the $\boldsymbol{k}_{sr}$ vector in this experiment, these components naturally form identical pairs. These pairs of

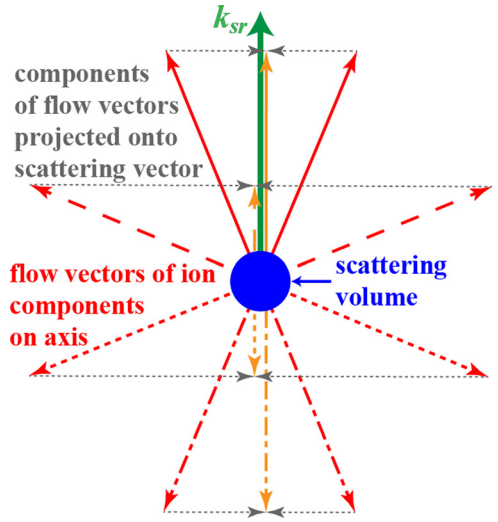


FIG. 9. Diagram of the Thomson scattering geometry at the array axis, showing the relative orientation of the stream velocity vectors and radial scattering vector ($k_{sr}$). The eight streams may be divided into four pairs (marked in orange) with equal components parallel to the radial scattering vector ($\vec{k}_{sr}$,).

streams are indicated by matching dash patterns of the red stream arrows in Fig. 9. For eight wires, the correct fit should require four geometrically constrained ion populations, the radial velocities of which will be scaled by the cosine of their angle from the scattering vector (orange vectors in Fig. 9).

The fit to the axial data is simpler; due to the cylindrical symmetry of the experiment, each flow should have the same axial velocity component ($\boldsymbol{v} \cdot \hat{\boldsymbol{k}}_{sz}$). This model is quite successful in reproducing the form of the spectra measured on axis. For this fit, the streams were modeled using an absolute radial velocity of $1.9 \times 10^5\,\mathrm{ms}^{-1}$, an axial velocity of $0.8 \times 10^5\,\mathrm{ms}^{-1}$ (again, directed towards the anode), and an ion temperature of 13 keV.

The fits presented in Fig. 8(c) correspond to a position roughly half way between the two described above. We have again fitted these spectra with four separate populations. This was necessary in order to match the spectral shape of the radial profile. These fits are however slightly more arbitrary due to the relaxed symmetry at this position. This spectrum is however illustrative of the general trend of the populations as they propagate towards the axis. Some evidence of the incoming stream is still discernable; unlike the spectrum seen on axis, the radial spectrum at this position is not symmetric. The "incoming" stream which makes up the right edge of this spectrum has a lower temperature than the "outgoing" stream feature on the far side. The subpopulations used to produce this fit are plotted as blue lines. The most important of these are the outer profiles—the inner profiles are more arbitrary. For the incoming flow, we have modeled a radial velocity of $\sim 1.9 \times 10^5\,\mathrm{ms}^{-1}$ and a temperature of $\sim$5 keV. For the flow which has already passed through the axis, we have a residual radial recession velocity of $\sim -1.4 \times 10^5\,\mathrm{ms}^{-1}$ and a temperature of $\sim$15 keV. As was seen in the other fits, the axial spectrum is much narrower than the radial. We have therefore modeled all four spectra with approximately the same axial velocity, in this case $\sim 0.5 \times 10^5\,\mathrm{ms}^{-1}$, again directed towards the anode. This fit appears to match the observed width of the axial spectrum reasonably well, providing further evidence in support of our estimate of the ion temperature.

It is interesting to note that the radial velocity on axis is actually slightly faster than the radial velocity of the incoming streams. The plasma on axis also has significant axial velocity, which further adds to its total kinetic energy. It seems likely this disparity in the kinetic energy of the incoming and on-axis plasma is due to an early variation in the ablation velocity; the plasma on axis was launched $\sim$20 ns earlier (based on a time of flight argument) than plasma at $r = 4$ mm. Fig. 11(b) shows a plot of the variation of measured approach velocity with time; previous TS measurements at 120 ns (Ref. 20) indicated an ablation velocity of $\sim 1.6 \times 10^5\,\mathrm{ms}^{-1}$, and the data recorded 140 ns, presented in Section IV A of this paper, indicate the ablation velocity has by that time reduced to $\sim 1.2 \times 10^5\,\mathrm{ms}^{-1}$, so there is strong evidence in support of a time-varying ablation velocity.

The presence of the axial deflection of the ablation streams means that the toroidal magnetic field is already present, even at this early time. The ratio of the axial to radial velocity on axis is substantially smaller at this time, indicating that this field is less dynamically significant at earlier times. This effect is discussed further in Section V B.

### C. Thomson spectrum at 150 ns

The Thomson scattering spectrogram shown in Fig. 6(c) was captured at $\sim$150 ns, around the time at which the dense precursor column starts to form.[31] Spectral profiles extracted from this spectrogram are presented in Fig. 10(a). Looking first at the spectra from the radially sensitive fibers, we see that the outer $\sim$5 fibers have very simple spectral structures. These are made up of narrow, single, red-shifted peaks, which correspond directly to the incoming ablation streams. These peaks are almost entirely dominant; there is very little evidence of the high temperature background populations seen at 100 ns and 140 ns, suggesting that the plasma is no longer interpenetrating out to these radii. Fitting these peaks yields an ion temperature of $\sim$500 eV and an incoming radial flow velocity of $\sim 1.1 \times 10^5\,\mathrm{ms}^{-1}$, continuing the trend of the incoming ablation streams to become cooler and slower with time (see Fig. 11(b)). Turning to the axially sensitive spectra, for these outer scattering volumes, the form of the spectral profiles is again very simple. The temperatures needed to fit these spectra are the same as for the radial spectra, and the centers of these spectra are un-shifted, indicating that the bulk axial velocity of the incoming ablation streams is negligible.

In the following discussion, we refer to the numbering of the scattering volumes as given in Fig. 10(a) between the two columns of plots. The incoming ablation stream is seen to extend through volumes #1–5, with approximately constant velocity and temperature, up to a radius of $\sim$2 mm from the array axis. Interaction of the flows appears to begin around volumes #6 and 7, where we see evidence of a second ion-population in the radial spectrum. Over the range from

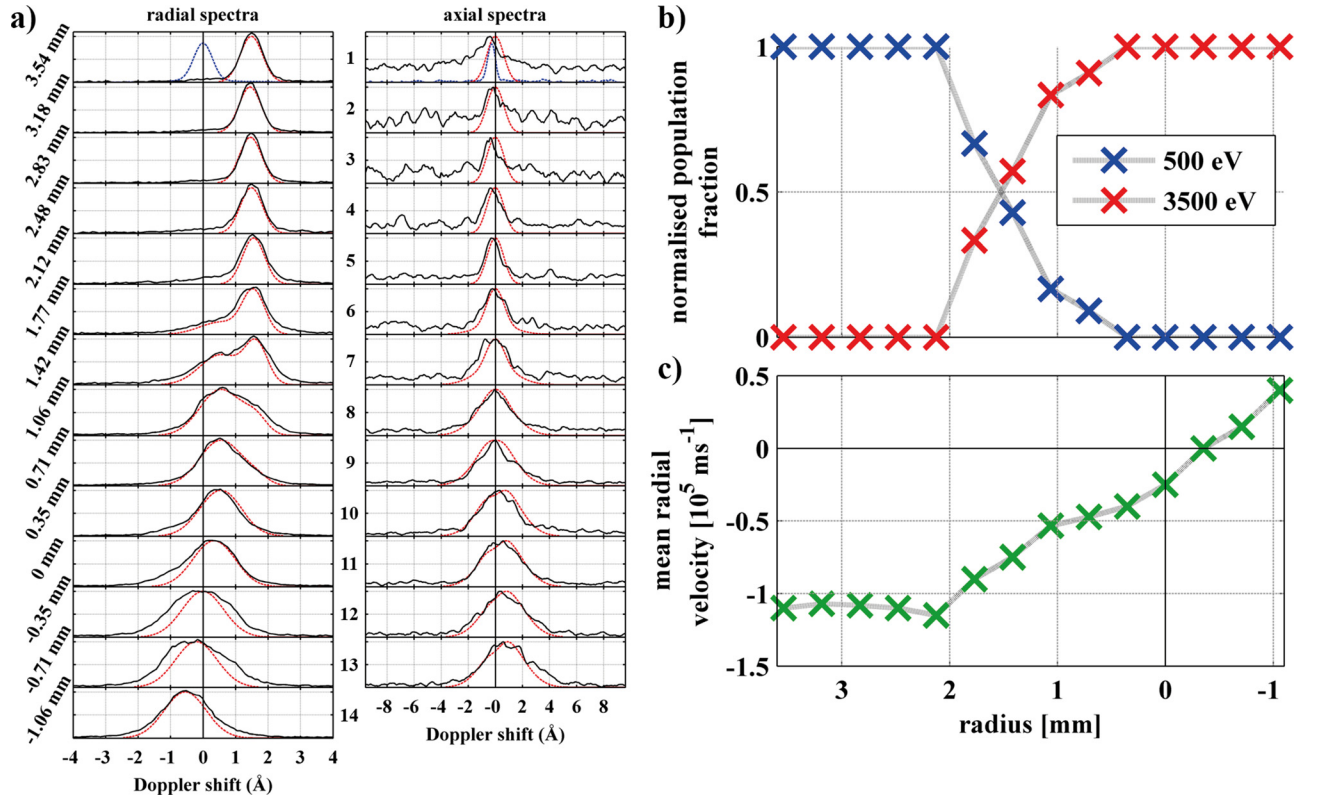


FIG. 10. Thomson scattering measurement at 150 ns. (a) Individual spectra extracted from the Thomson scattering spectrogram recorded at 150 ns (Fig. 6(c)). Black lines are experimental spectra, blue lines show spectrum of un-scattered laser line used for calibration. Red lines are fits to the Thomson scattering data. It should be noted that the horizontal scales used on these plots are half as wide as those used in Figs. 7 and 8. (b) Plot of relative contribution of 500 eV and 3500 eV populations to fits seen in (a). (c) Average velocity of populations used to fit TS data in (a).

volumes #6–#9, which corresponds to a radial range of ~1 mm, the incoming flow appears to undergo a transition to higher temperature and lower velocity. At fiber 9, at $r \sim 0.7$ mm, the flow can be approximately fitted with a single ion population of temperature of ~3500 eV and a radial velocity of $\sim 0.4 \times 10^5 \text{ms}^{-1}$. In Fig. 10, the radial spectra from positions #6 to 9 have been fitted by mixing together varying proportions of the pre and post-transition populations. Fig. 10(b) shows plots of the relative density of these two component populations with radius. The jump over this "shock" represents an abrupt jump in temperature of ~×7 and fall in velocity of ~×2.5; the axial velocity of the flow after the shock remains almost negligible. The absence of ion-acoustic peaks in the TS spectra on both side of the "shock" indicates that $T_i \gg \bar{Z}T_e$, and therefore we may estimate the pre and post "shock" Mach numbers ($M$) based on a $T_i$ dominated ion-sound-speed. This method produces an estimated incoming $M \sim 7$ and post shock $M \sim 1$.

Approaching the axis of the array, at fiber 11/12, the flow velocity continues to decrease (the mean population weighted velocity is plotted in Fig. 10(c)), reaching ~0 at position #12, which is approximately on axis. On the far side of the axis, the flow velocity starts to increase in the opposite direction. This ramped change in velocity across the radius of the central region indicates that the plasma here is undergoing compression. The ion-temperature of the plasma in this region remains fairly constant across its width, at around 3–3.5 keV, indicating that thermal conduction in the region is likely to be faster than the rate of kinetic-energy thermalization. Within the central region, we see some evidence of axial flow, however this flow appears to be directed towards the cathode of the array, and the magnitude of the peak axial velocity is in this case substantially lower. Fits of fiber 12 axial data give a maximum axial velocity of $\sim 0.3 \times 10^5 \text{ms}^{-1}$. The absence of substantial axial flow implies that any toroidal magnetic field that might have been present earlier in time, as evidenced by measurements of axial deflection in the earlier TS data, has collapsed towards the array axis, due to some combination of radial compression and resistive annihilation.

The temperature of the post shock plasma quoted above was found by fitting to the widths of the axial spectra measured from volumes #10–13. It should be noted that these widths do not fit the radially-sensitive spectra that well. It is possible that this inconsistency may reflect some anisotropy in the ion velocity distribution, however this seems unlikely. Instead it seems possible that a combination of the rapid spatial variation of the bulk radial velocity of the ion flows in this region and the finite size of the scattering volumes has led to the fibers sampling plasma with a range of bulk velocities. This, in effect, will smear out the width of the measured spectrum, giving the appearance of greater ion-temperature. This "sampling width" effect could also have contributed to the slightly strange forms of the radial scattering peaks for volumes # 6–8, as these spectra may have both post and pre-shock components contributing to each signal.

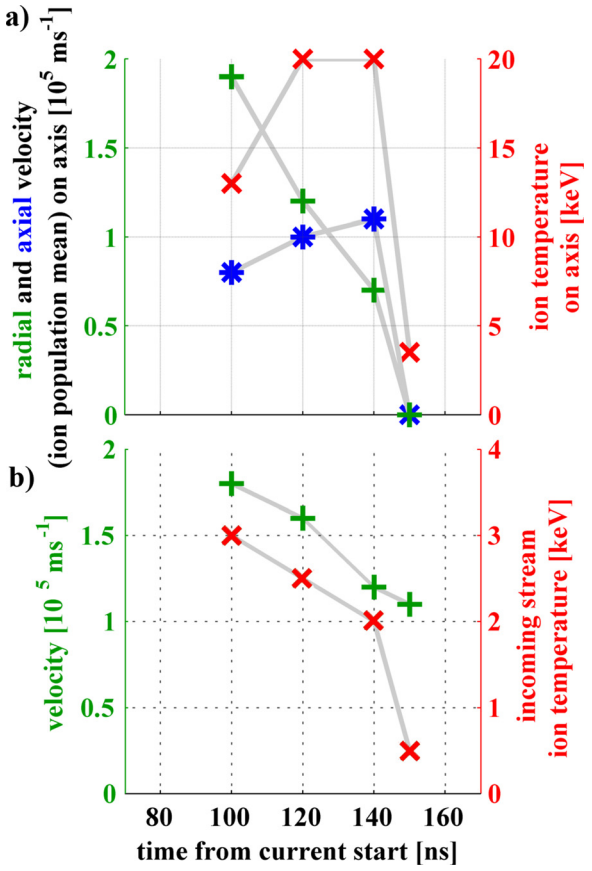


FIG. 11. Plots of data from Table I. (a) Variation with time of the mean radial (green + and axial (blue *) velocities and ion temperatures (red ×) of interpenetrating ion populations on axis. (b) Plots of variation of measured incoming velocity (green +) and temperature (red ×) of ablation streams approaching the interaction region. Measured from TS data presented in Sec. IV and in Ref. 20.

TABLE I. Summary of key experimental measurements. Results for 120 ns are taken from Ref. 20. Selected data from this table are plotted in Figs. 5 and 11.

Velocities and temperatures of incoming streams

| Time [ns] | $\|v_r\|$ [ms$^{-1}$] | $T_i$ [keV] |
|---|---|---|
| 100 | $1.8 \times 10^5$ | 3 |
| 120 | $1.6 \times 10^5$ | 2.5 |
| 140 | $1.2 \times 10^5$ | 2 |
| 150 | $1.1 \times 10^5$ | 0.5 |

Plasma parameters on axis

| Time [ns] | $n_e$ [cm$^{-3}$] | $\|v_r\|$ [ms$^{-1}$] | $v_z$ [ms$^{-1}$] | $T_i$ [keV] |
|---|---|---|---|---|
| 100 | $4 \times 10^{17}$ | $1.9 \times 10^5$ | $0.8 \times 10^5$ | 13 |
| 120 | $6 \times 10^{17}$ | $1.2 \times 10^5$ | $1 \times 10^5$ | 20 |
| 140 | $1 \times 10^{18}$ | $0.7 \times 10^5$ | $1.1 \times 10^5$ | 20 |
| 150 | $4 \times 10^{18}$ | 0 | 0 | 3.5 |

## V. DISCUSSION

A summary of the key experimental measurements presented in Sections III and IV is provided in Table I to ease reference during the following discussions.

### A. Collisional dynamics

The analysis of the data collected in these experiments clearly indicates that the collisional dynamics of the tungsten ablation streams changes significantly over the timescale of the measurements. Up to at least 140 ns into the current drive, the TS measurements show that the ablation streams are interpenetrating across the array axis, and the dynamics of that interpenetration can be leveraged to gain further insights into the likely plasma parameters. In the interpretation of similar interferometry measurements presented in Ref. 19, it was asserted that ion-ion collisions dominate the interaction dynamics. That statement was based on the conclusion that at the expected $T_e \sim 20$ eV (this parameter was not directly measured), the ion-electron collision rate would be much smaller than the corresponding ion-ion rate. That conclusion was based on calculations using an incorrect estimate for the ion-ion coulomb logarithm ($\lambda_{ii}$) (an incorrect engineering formula was taken from Ref. 37, see Appendix of Ref. 11 for notes on the correction). Although this error has no impact on the validity of the experimental data presented in Ref. 19, calculations using the corrected equation for $\lambda_{ii}$ suggest that a higher electron temperature is required than was previously estimated in order for the expected dynamics of the plasma to be consistent with those observed.

The experimental evidence presented in this paper, combined with data presented previously,[19,20] strongly supports the view that the collisional interactions near the array axis at early times ($t < 140$ ns) must be dominated by ion-ion collisions. The interferograms presented in Fig. 4 clearly and consistently show well defined, focused ablation streams extending right up to the edge of the "interaction region" (see Fig. 1(b)). Upon crossing the boundary of the "interaction region," these streams rapidly diverge to form an azimuthally isotropic, smooth distribution of electron density. The ions carry the momentum of the ablation streams and it is therefore their motion which determines the mass and, via quasi-neutrality, the electron density distribution of the plasma. In order to explain the smooth structure and lack of ablation stream imprint seen in the interferometry data, the ions must undergo rapid scattering upon entering the "interaction region." The TS data provide further evidence of strong scattering. For Thomson scattering observed along observation vector $\vec{k}_{oz}$ (see Fig. 1(d)) for diagram), the form of the TS ion feature is sensitive only to the transverse diffusion of the ion velocity distribution and the ion bulk axial velocity, whilst for scattering observed along $\vec{k}_{or}$, it is sensitive only to the parallel diffusion and radial velocity of the ion population. The rapidly rising, matched values of $T_i$ used to fit spectra measured simultaneously along both these directions (see Sections IV A and IV B) indicate that the ion streams are undergoing significant, simultaneous parallel and transverse diffusions. The data further indicate that the observed slowing-down mean free path (MFP) for the ion stream, $l_s^{i\backslash\beta}$ must be of the same order as the parallel and transverse diffusion MFPs, $l_{\|}^{i\backslash\beta}$ and $l_{\perp}^{i\backslash\beta}$, as these processes are observed to occur over similar spatial scales (superscript

$i\backslash\beta$ indicates collisions of stream ions, $i$, with scattering populations $\beta = i$ for ions or $e$ for electrons).

Taking the ratio of the expected theoretical values for $l_s^{i\backslash\beta}$ and $l_\perp^{i\backslash\beta}$ gives the following expression:[37,38]

$$\frac{l_\perp^{i\backslash\beta}}{l_s^{i\backslash\beta}} = \frac{\left(1+\frac{m_i}{m_\beta}\right)\psi(x^{i\backslash\beta})}{2\left[\left(1-\frac{1}{2x^{i\backslash\beta}}\right)\psi(x^{i\backslash\beta})+\psi'(x^{i\backslash\beta})\right]} \tag{3}$$

$$\psi(x^{\alpha\backslash\beta}) = \frac{2}{\sqrt{\pi}}\int_0^{x^{\alpha\backslash\beta}} te^{-t}dt\,, \quad x^{\alpha\backslash\beta} = \frac{m_\beta v_\alpha^2}{2k_B T_\beta}\,.$$

In this equation, $\psi(x^{\alpha\backslash\beta})$ is the velocity potential for the interaction.[38] Given the lack of obvious ion-acoustic peaks in the TS data, we place an extremely generous upper limit on the possible electron temperature of $T_e < 400\,\text{eV}$. From this, we can deduce that for all possible values of $T_e$, $l_\perp^{i\backslash e}/l_s^{i\backslash e} \gg 1$ (e.g., $T_e = 10\,\text{eV}$ $l_\perp^{i\backslash e}/l_s^{i\backslash e} = 500$, $T_e = 400\,\text{eV}$, $l_\perp^{i\backslash e}/l_s^{i\backslash e} = 12$). This implies that transverse scattering of the ions due to ion-electron interactions should be negligible (i.e., these interactions may be treated as a simple drag force). If ion-electron collisions are dominant, then the ablation streams should remain well-defined and focused all the way to the array axis, and their ion temperatures should not increase significantly as they slow down. This is not observed; instead, as the streams decelerate, they appear to undergo strong directional scattering and rapid ion heating. For ion-ion collisions, $l_\perp^{i\backslash i}/l_s^{i\backslash i} \sim 1$, and therefore ion heating and scattering processes should occur on the same spatial scale as the slowing down of the streams. The observed interaction dynamics is therefore consistent only with plasma parameters under which the effects of ion-ion interactions dominate over the ion-electron interactions.

Having established that the observed nature of the interactions strongly indicates the dominance of ion-ion collisions, we will now investigate the plausibility of the plasma parameters required to produce the condition where the ion-electron mean free path exceeds the ion-ion mean free path ($l_s^{i\backslash e}/l_s^{i\backslash i} > 1$). The characteristic length scale for classical collisional deceleration of a directed stream of ions is given by the following well know expression:[37,38]

$$l_s^{i\backslash\beta} = \frac{1}{(1+m_i/m_\beta)\psi^{i\backslash\beta}}\frac{m_i^2 v_i^4}{4\pi\bar{Z}_\beta^2\bar{Z}_i^2 e^4\lambda_{i\beta}n_\beta}, \tag{4}$$

where $m$, $v$, and $\bar{Z}$ are, respectively, the mass, velocity, and ionization state, $\lambda_{i\beta}$ is the coulomb logarithm and $\psi^{i\backslash\beta}$ is the velocity potential. The ion-ion coulomb logarithm used in these calculations was calculated using the following equation[38] (this is a correction with respect to the approximated expression given in Ref. 37, which was used previously for interpretation in Ref. 19):

$$\lambda_{ii} = \ln\left(\frac{m_i v_i^2}{2Z^2e^3}\sqrt{\frac{kT_e}{4\pi n_e}}\right). \tag{5}$$

The coulomb logarithm for the ion-electron collisions was calculated as previously using the formulae provided in Ref. 37. Over the parameter range of interest, $\lambda_{ie} \sim 3$–$7$ and $\lambda_{ii} \sim 8$–$11$. Taking the ratio of the MFPs for slowing through collisions with ions and electron gives the following expression:

$$\frac{l_s^{i\backslash e}}{l_s^{i\backslash i}} = \frac{2}{\left(1+\frac{m_i}{m_e}\right)}\frac{\psi(x^{i\backslash i})}{\psi(x^{i\backslash e})}\frac{\lambda_{ii}}{\lambda_{ie}}\bar{Z}. \tag{6}$$

The ranges quoted for the coulomb logarithms above imply that the ratio $\lambda_{ii}/\lambda_{ie}$ remains of order unity; the ratio of MFPs is therefore controlled largely by the ratio $\psi(x^{i\backslash i})/\psi(x^{i\backslash e})$, which must compensate for the large ion-electron mass discrepancy factor ($m_i/m_e \sim 3.4\times10^5$). The ratio $\psi(x^{i\backslash i})/\psi(x^{i\backslash e})$ is in turn largely controlled by $T_e$ and it is therefore possible to estimate a lower bound for $T_e$ based on the condition that consistency with the experimental data requires $l_s^{i\backslash e}/l_s^{i\backslash i} > 1$.

Starting with the earliest Thomson scattering measurement, at 100 ns, the incoming ablation stream velocity $v_i$ is $\sim 1.8\times10^5\ \text{ms}^{-1}$, the $T_i$ on axis is $\sim$13 keV, and $n_e \sim 4\times10^{17}\,\text{cm}^{-3}$. The width of the "interaction region" at this time is estimated from the Thomson scattering spectra in Fig. 8 to be $\sim$8 mm. Making the assumption that ion-ion collisions do indeed dominate, $\bar{Z}$ is adjusted to achieve $l_s^{i\backslash i} \sim 8\,\text{mm}$; for the above parameters, this requires $\bar{Z} \sim 15$ . The electron temperature is then adjusted so that $l_s^{i\backslash e}/l_s^{i\backslash i} > 1$. This is the point at which the ion collisions become equally important to the electron collisions. The condition is reached at $T_e > 30\,\text{eV}$. These values for $\bar{Z}$ and $T_e$ seem reasonably consistent. Retrieving $\bar{Z} = 15$ as the equilibrium ionization state solution to the Saha equations for tungsten requires setting $T_e = 22$ eV. This should be treated as a lower bound for the required temperature, as the Saha model assumes the plasma has reached local thermodynamic equilibrium (LTE), which seems unlikely for this plasma. It is in fact possible that $T_e$ may be significantly higher. For $T_e = 30\,\text{eV}$, $\bar{Z}T_e = 450\,\text{eV}$, which is consistent with the absence of ion-acoustic peaks in the TS data (this constrains the plasma such that $T_i > \bar{Z}T_e$); the $T_i$ used to fit the incoming ablation stream for this measurement was $\sim$3 keV.

At 140 ns, the plasma parameters have somewhat evolved. On axis, $T_i \sim 20\,\text{keV}$, the incoming ablation stream velocity has fallen to $1.2\times10^5\,\text{ms}^{-1}$ and $n_e$ has increased to $2\times10^{18}\,\text{cm}^{-3}$ on axis. The observed slowing down scale length, inferred from the TS data in Fig. 7, has reduced a little to $\sim$4 mm. Under these conditions, $\bar{Z} > 8$ is required to reproduce $l_s^{i\backslash i} < 4\,\text{mm}$, and to reach $l_s^{i\backslash e}/l_s^{i\backslash i} > 1$ we again require a minimum $T_e > 30$ eV.

It can be argued that reaching the point where ion-ion collisions dominate is somewhat inevitable. The electrons are highly mobile within the plasma, and thermalize rapidly, such that they may be treated as a single population. If we start from a cold electron population, the incoming streams will friction heat the electron population to the point where $l_s^{i\backslash e} > l_s^{i\backslash i}$ and ion-ion collisions start to become dominant. The increasing electron temperature will also drive up the $\bar{Z}$ of the plasma, further increasing the strength of the ion-ion

collisions with respect to the electron collisions. At this point, the electron population will have become effectively "transparent" to the incoming flows and the heating rate will drop. If the plasma cools, $l_s^{i\backslash e}$ will decrease until a new equilibrium is reached between the various losses and frictional heating. The radiative cooling rate for the tungsten plasma is likely to be rapid. Estimates taken from Ref. 39 for a $T_e = 100\,\text{eV}$ tungsten plasma (this is the lowest temperature for which the cooling rate is available in Ref. 39) suggest a cooling time-scale on the order of $\sim$1 ns. In order for our steady-state model to be viable, we need to show that the frictional heating rate is potentially fast enough to compete with this cooling rate. Equating the rate of change of internal energy to the classical electron-ion frictional heating power gives the following expression:[38,40]

$$\begin{aligned} \frac{3}{2} n_e k_B \frac{dT_e}{dt} &= F \cdot v_i = m_e n_e \nu_{ei} v_i^2 \\ \tau_{ei} = \nu_{ei}^{-1} &= \frac{3}{4}\left(\frac{m_e}{2\pi}\right)^{\frac{1}{2}} \frac{(T_e k_B)^{3/2}}{\lambda_{ei} e^4 \bar{Z}^2 n_i}. \end{aligned} \tag{7}$$

Rearrangement of this expression produces an estimate for the characteristic heating rate

$$\begin{aligned} \frac{dT_e}{dt} &= \frac{8\sqrt{2\pi m_e} e^4}{9 k_B^{5/2}} \frac{\lambda_{ei} \bar{Z} n_e v_i^2}{T_e^{3/2}} \\ \frac{dT_e}{dt} &= 1.1 \times 10^{-21} \cdot \frac{\lambda_{ei} \bar{Z} n_e v_i^2}{T_e^{3/2}}\ [\text{CGS/eV}]. \end{aligned} \tag{8}$$

Inserting parameters for the plasma on axis at 100 ns, $v_i = 1.8 \times 10^7\,\text{cms}^{-1}$, $n_e = 4 \times 10^{17}\,\text{cm}^{-3}$, and taking the approximations $\lambda_{ei} = 10$ and $\bar{Z} = 10$ and setting $T_e = 30\,\text{eV}$, we retrieve a heating rate of $dT_e/dt \sim 90\,\text{eV ns}^{-1}$. This is rapid, and suggests that frictional heating should be able to keep up with radiative cooling at this temperature and density.

The arguments presented here allow us to construct a model where the classical collisional interactions of the streams are consistent with the dynamics observed in experiments. Direct measurements of the electron temperature of the plasma are required in order to properly verify these arguments, perhaps via measurements of the electron component of the TS spectrum, or via spectroscopic techniques. The calculations presented here suggest that the required plasma conditions, particularly a sufficiently high electron temperature, are certainly not impossible. An assessment of whether more complex processes are at work, e.g., kinetic effects, particularly during the early stages of the stream interactions, goes beyond the scope of the current paper but merits future attention.

### B. Magnetic field in the interaction region

In previous experiments, we saw indirect evidence of the presence of a static toroidal magnetic field in the "interaction region" around the array axis.[20] As the ion populations approached the axis, they were observed to acquire an axial velocity directed towards the array anode. After passing through the axis, this axial velocity was observed to reduce again back towards zero. This "S" shaped trajectory (see Fig. 12 for diagram) is consistent with the $J \times B$ force structure one would expect a static toroidal field to impart on the ion stream as it travels through the array axis. The strength of the field was estimated in Ref. 20 based on arguments related to the ion-gyroradius required to produce the observed deflection angle at the axis. For this estimate, it was assumed the radial width of the magnetized region was $r = 1.65\,\text{mm}$, which gave an estimated $\bar{Z}|B| \sim 130\,\text{T}$. The magnetic field of $|B| \sim 20\,\text{T}$ was estimated based on $\bar{Z} = 6$.

The data presented in this paper further support the conclusion that a static magnetic field is present around the axis at early times in these experiments. Analysis of the new Thomson scattering data presented in Sections IV A and IV B revealed similar axial deflections of the ion-populations at both 100 and 140 ns. Further experiments have also been conducted, including one where the anode and cathode were reversed with respect to the TS scattering geometry. In every experiment, the deflection of the ion-populations was towards the anode, and always with the S-type trajectory depicted in Fig. 12. Furthermore, as Fig. 1(c) shows, the scattering volumes from which the TS spectra are collected are actually distributed in the axial direction (over $\sim$11 mm), as well as in the radial direction. In each experiment, all of these axially distributed scattering volumes show the same anode wise deflection. This is strong evidence against the measured deflections being associated with small scale variations in the axial velocity of the precursor plasma. Finally, as we have already discussed, magnetic field advection has been measured directly in wire array ablation plasma flows previously.[21,25,26] If this measured field were to be accrued about the axis, then its measured direction would be consistent with the required force structure. Given the low degree of collisionality at early times, it is difficult to explain this phenomenon in any other way.

At 100 ns (see Section IV A), the radial velocity on axis is $1.9 \times 10^5\,\text{ms}^{-1}$ and the axial velocity is $0.8 \times 10^5\,\text{ms}^{-1}$. This gives a flow angle ($\text{atan}(v_z/v_r)$) on axis of 22.5°. In our previous experiment,[20] the flow angle on axis at 120 ns was measured as 45°. At 140 ns (see Section IV B), the axial velocity is $1.1 \times 10^5\,\text{ms}^{-1}$ and the radial velocity is just

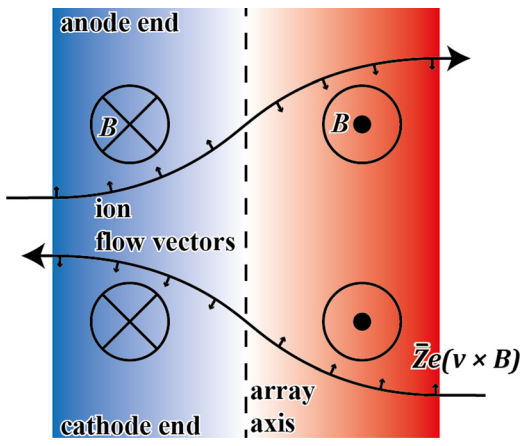


FIG. 12. S-shaped trajectory of ions is consistent with a toroidal magnetic field about the array axis. Small arrows indicate direction of Lorentz force.

$0.7 \times 10^5\,\mathrm{ms}^{-1}$, giving a deflection angle of 60°. The angle of deflection ($\theta$) and spatial scale of the deflection ($d$) are used to estimate the magnetic field about the axis using the following equation:

$$B\bar{Z} = \frac{|v|m_i c}{ed}\sin\theta\,[\mathrm{CGS}]. \tag{9}$$

This equation is based on the same ion-gyroradius argument used in Ref. 20. The estimate in Ref. 20 was based on an estimate of $\bar{Z} = 6$. Corrected calculations of the collisional scale length (Section V A) suggest that this value for $\bar{Z}$ may be too low. This calculation also more than likely underestimated the range over which the deflection takes place; the deflection process had already begun by the point of the first measurement. Based on the new information presented in this paper, we make the following estimates. At 100 ns, using $v = 1.8 \times 10^5\,\mathrm{ms}^{-1}$ and $d = 2\,\mathrm{mm}$, we estimate $B\bar{Z} \sim 70\,\mathrm{T}$; at 120 ns, using $v = 1.6 \times 10^5\,\mathrm{ms}^{-1}$ and $d = 2\,\mathrm{mm}$ we estimate $B\bar{Z} \sim 110\,\mathrm{T}$. At 140 ns, using $v = 1.2 \times 10^5\,\mathrm{ms}^{-1}$ and $d = 2\,\mathrm{mm}$, we estimate $B\bar{Z} \sim 110\,\mathrm{T}$. Assuming $\bar{Z} \sim 10$, the magnetic field in this region is $B \sim 7$–$11\,\mathrm{T}$.

In order for a magnetic field to produce a force on a stream of ions, the field must be "static" with respect to the ion flow velocity (i.e., static in the laboratory reference frame). The toroidal geometry of the magnetic field implied by the measurements at 100 and 140 ns (and in previous experiments at 120 ns (Ref. 20)) will naturally try to induce a collapse towards the array axis. In order for the field to be static, it must be frozen into the electron component of the plasma, and the column of plasma on axis must provide some force in order to resist the magnetic pinching. This force will be provided by a combination of the thermal pressure of the ion populations and by the residual, out-going ram pressure of the ion streams after they have penetrated through the array axis. The ion populations are tied spatially to the electron population via the electrostatic forces that enforce quasi-neutrality, and can therefore act to prevent the collapse of the magnetic field. As time goes on and the ion-ion collision scale length decreases, the ram pressure of the streams will gradually be redistributed; the outwardly directed component will gradually disappear and an inwardly directed, compression force will come to dominate. As the ion-electron equilibration time decreases, the ions will be able to cool more effectively, leading to a reduction in their temperature and thus a fall in thermal pressure. At 150 ns, the ion temperature of both the ablation streams and plasma on axis is substantially reduced, and it appears that the ablation streams are no longer able to penetrate through the axis. The combination of these effects will gradually reduce the thermal and ram pressure available to support the central magnetized column. The magnetic pressure acting on the column will then contribute towards its collapse. Estimates of the plasma $\beta$ support this narrative. The thermal pressure of the plasma should be dominated by the ion component ($\bar{Z}T_e \ll T_i$), so the plasma $\beta$ can be estimated as follows:

$$\beta = \frac{8\pi n_i k_B T_i}{B^2} = \frac{8\pi \bar{Z} n_e k_B T_i}{(\bar{Z}B)^2}\ [\mathrm{CGS}]. \tag{10}$$

Using the parameters discussed in Section V A for the plasma at 140 ns ($T_i \sim 20$ keV , $n_e \sim 1 \times 10^{18}\,\mathrm{cm}^{-3}$ (density in the magnetized region) $\bar{Z} \sim 8$ ), we retrieve $\beta \sim 5$, which indicates that at this time, the thermal pressure is very much dominant. At 150 ns, although the electron density on axis has increased by $\sim\times 2$, the width of the density distribution has decreased substantially, leading to only a small increase in density in the region around the axis where the magnetic field resides and the ion temperature of the plasma has fallen significantly, to around $\sim 3.5$ keV. These two effects lead to an estimate (assuming the previous magnetic field was still present) of $\beta \sim 1$, which suggests the magnetic field should be dynamically significant at this time.

This interpretation is supported by the absence of material in the inter-stream segments in the interferometry data at 150 ns and 160 ns. The ablation streams at this late time are highly focused, so that it seems unlikely that the collapse of the plasma column could be completely explained by the increasing ram pressure of the ablation stream; were this the case we would expect to see some "trailing" high temperature plasma in the inter-stream regions.

### C. Evolution of ablation streams properties

The plasma parameters of the ablation streams are seen to vary significantly with time. These variations are shown graphically in Fig. 11(b). At 100 ns, the incoming ablation streams were measured as having a $T_i \sim 5000$ eV and an incoming radial velocity of $\sim 1.9 \times 10^5\,\mathrm{ms}^{-1}$. In a similar experiments conducted previously,[20] the temperature and velocity of the incoming streams at 120 ns were measured to be $\sim 1.6 \times 10^5\,\mathrm{ms}^{-1}$ and 2000–3000 eV, respectively. At 140 ns, $T_i$ was measured at 3000 eV and the velocity at $\sim 1.2 \times 10^5\,\mathrm{ms}^{-1}$. Finally at 150 ns, the temperature and velocity of the ablation streams has fallen further to $\sim 500$ eV and $\sim 1.1 \times 10^5\,\mathrm{ms}^{-1}$, respectively.

The variation of ablation velocity with time has been suspected for some time,[30] and has been noted in previous TS measurements.[33,34] The observation of a strong temporal variation in the ion temperature of the incoming streams is more novel. These measurements suggest that some mechanism is heating the plasma ablated by the wire cores, either as it is launched, or as it travels from the wire cores to the array axis. The decrease in observed temperature with time may be explained by increased radiative cooling of the streams as their densities increase with time. The cooling rate for the ions in the ablation streams will be linked to the ion-electron equilibration time, which will decrease with increasing stream density. We would therefore expect the ablation streams reaching the axis at later times to have a lower temperature. While this explanation is consistent with the data, further calculations of the stream cooling rates would be required in order to properly assess this model. It is very much less clear as to what mechanism is heating the ablation streams to such a high initial ion temperature. Further work will be required to understand this phenomenon.

## VI. CONCLUSION

The data set presented in this paper provides a detailed view of the changes in the interaction dynamics of the radially convergent ablation streams during the early phase of tungsten wire array evolution.

The measurements made at 100 ns clearly demonstrate flow interpenetration through the array axis at early time, while the combination of new measurements at 140 ns with previous measurements at 120 ns (Ref. 20) illustrates the gradual evolution of the inter-stream collisionality as the density of the plasma on axis increases.

The observed evolution of the plasma density and ion temperature is consistent with collisions dominated by ion-ion interactions. For this to be the case, we require a $\bar{Z} \sim 15$ and electron temperature $T_e > 30$ eV. This electron temperature is likely to be supported by friction heating of the electron population by the incoming ablation streams. This heating will be limited to the electron temperature at which the electron population becomes "transparent" to these incoming streams, which will occur as the electron thermal velocity begins to exceed the incoming stream velocity. It seems likely that the actual electron temperature is controlled by a balance between incoming stream velocity and the radiative cooling rate. Further work is required to better understand this process, in particular, direct measurements of $T_e$ would be extremely useful in order to better constrain our models.

Further evidence of the magnetization of the broad precursor plasma column is provided by measurements of ablation stream deflections at 100 and 140 ns. The magnetized column is observed to have disappeared by 150 ns, and this is interpreted as being the result of the collapse of an ion mediated pressure, which acts to support the inward pressure of the magnetized electron population through electrostatic forces at earlier times.

Finally, we see evidence that the ablation streams are heated to high temperatures at launch. This is somewhat surprising and an understanding of the mechanism driving this will require further experimental investigation.

## ACKNOWLEDGMENTS

This work was supported in part by EPSRC Grant No. EP/G001324/1 by DOE cooperative Agreement Nos. DE-F03-02NA00057 and DE-SC-0001063 and by Sandia National Laboratories.

[1]O. Rancu, P. Renaudin, C. Chenais-Popovics, H. Kawagashi, J. Gauthier, M. Dirksmöller, T. Missalla, I. Uschmann, E. Förster, O. Larroche, O. Peyrusse, O. Renner, E. Krouský, H. Pépin, and T. Shepard, Phys. Rev. Lett. **75**, 3854 (1995).
[2]Y. Kuramitsu, Y. Sakawa, T. Morita, C. D. Gregory, J. N. Waugh, S. Dono, H. Aoki, H. Tanji, M. Koenig, N. Woolsey, and H. Takabe, Phys. Rev. Lett. **106**, 175002 (2011).
[3]H.-S. Park, D. D. Ryutov, J. S. Ross, N. L. Kugland, S. H. Glenzer, C. Plechaty, S. M. Pollaine, B. A. Remington, A. Spitkovsky, L. Gargate, G. Gregori, A. Bell, C. Murphy, Y. Sakawa, Y. Kuramitsu, T. Morita, H. Takabe, D. H. Froula, G. Fiksel, F. Miniati, M. Koenig, A. Ravasio, A. Pelka, E. Liang, N. Woolsey, C. C. Kuranz, R. P. Drake, and M. J. Grosskopf, High Energy Density Phys. **8**, 38 (2012).
[4]J. S. Ross, S. H. Glenzer, P. Amendt, R. Berger, L. Divol, N. L. Kugland, O. L. Landen, C. Plechaty, B. Remington, D. Ryutov, W. Rozmus, D. H. Froula, G. Fiksel, C. Sorce, Y. Kuramitsu, T. Morita, Y. Sakawa, H. Takabe, R. P. Drake, M. Grosskopf, C. Kuranz, G. Gregori, J. Meinecke, C. D. Murphy, M. Koenig, A. Pelka, A. Ravasio, T. Vinci, E. Liang, R. Presura, A. Spitkovsky, F. Miniati, and H.-S. Park, Phys. Plasmas **19**, 056501 (2012).
[5]N. L. Kugland, D. D. Ryutov, P.-Y. Chang, R. P. Drake, G. Fiksel, D. H. Froula, S. H. Glenzer, G. Gregori, M. Grosskopf, M. Koenig, Y. Kuramitsu, C. Kuranz, M. C. Levy, E. Liang, J. Meinecke, F. Miniati, T. Morita, A. Pelka, C. Plechaty, R. Presura, A. Ravasio, B. A. Remington, B. Reville, J. S. Ross, Y. Sakawa, A. Spitkovsky, H. Takabe, and H.-S. Park, Nat. Phys. **8**, 809 (2012).
[6]C. M. Huntington, F. Fiuza, J. S. Ross, A. B. Zylstra, R. P. Drake, D. H. Froula, G. Gregori, N. L. Kugland, C. C. Kuranz, M. C. Levy, C. K. Li, J. Meinecke, T. Morita, R. Petrasso, C. Plechaty, B. A. Remington, D. D. Ryutov, Y. Sakawa, A. Spitkovsky, H. Takabe, and H.-S. Park, Nat. Phys. **11**, 173 (2015).
[7]H.-S. Park, C. M. Huntington, F. Fiuza, R. P. Drake, D. H. Froula, G. Gregori, M. Koenig, N. L. Kugland, C. C. Kuranz, D. Q. Lamb, M. C. Levy, C. K. Li, J. Meinecke, T. Morita, R. D. Petrasso, B. B. Pollock, B. A. Remington, H. G. Rinderknecht, M. Rosenberg, J. S. Ross, D. D. Ryutov, Y. Sakawa, A. Spitkovsky, H. Takabe, D. P. Turnbull, P. Tzeferacos, S. V. Weber, and A. B. Zylstra, Phys. Plasmas **22**, 056311 (2015).
[8]D. D. Ryutov, F. Fiuza, C. M. Huntington, J. S. Ross, and H.-S. Park, Phys. Plasmas **21**, 032701 (2014).
[9]S. C. Hsu, E. C. Merritt, A. L. Moser, T. J. Awe, S. J. E. Brockington, J. S. Davis, C. S. Adams, A. Case, J. T. Cassibry, J. P. Dunn, M. A. Gilmore, A. G. Lynn, S. J. Messer, and F. D. Witherspoon, Phys. Plasmas **19**, 123514 (2012).
[10]E. C. Merritt, A. L. Moser, S. C. Hsu, J. Loverich, and M. Gilmore, Phys. Rev. Lett. **111**, 085003 (2013).
[11]E. C. Merritt, A. L. Moser, S. C. Hsu, C. S. Adams, J. P. Dunn, A. Miguel Holgado, and M. A. Gilmore, Phys. Plasmas **21**, 055703 (2014).
[12]A. L. Moser and S. C. Hsu, Phys. Plasmas **22**, 055707 (2015).
[13]I. H. Mitchell, J. M. Bayley, J. P. Chittenden, J. F. Worley, A. E. Dangor, M. G. Haines, and P. Choi, Rev. Sci. Instrum. **67**, 1533 (1996).
[14]S. V. Lebedev, D. Ampleford, A. Ciardi, S. N. Bland, J. P. Chittenden, M. G. Haines, A. Frank, E. G. Blackman, and A. Cunningham, Astrophys. J. **616**, 988 (2004).
[15]D. J. Ampleford, S. V. Lebedev, A. Ciardi, S. N. Bland, S. C. Bott, J. P. Chittenden, G. Hall, C. A. Jennings, J. Armitage, G. Blyth, S. Christie, and L. Rutland, Astrophys. Space Sci. **298**, 241 (2005).
[16]F. Suzuki-Vidal, S. V. Lebedev, M. Bocchi, M. Krishnan, G. Swadling, G. Burdiak, S. N. Bland, P. Grouchy, G. N. Hall, A. J. Harvey-Thompson, E. Khoory, L. Pickworth, J. Skidmore, J. P. Chittenden, K. Wilson-Elliot, R. Madden, and A. Ciardi, Shock Waves **22**, 249 (2012).
[17]F. Suzuki-Vidal, S. V. Lebedev, M. Krishnan, J. Skidmore, G. F. Swadling, M. Bocchi, A. J. Harvey-Thompson, S. Patankar, G. C. Burdiak, P. de Grouchy, L. Pickworth, S. J. P. Stafford, L. Suttle, M. Bennett, S. N. Bland, J. P. Chittenden, G. N. Hall, E. Khoory, R. A. Smith, A. Ciardi, A. Frank, R. E. Madden, K. Wilson-Elliot, and P. Coleman, High Energy Density Phys. **9**, 141 (2013).
[18]G. F. Swadling, S. V. Lebedev, N. Niasse, J. P. Chittenden, G. N. Hall, F. Suzuki-Vidal, G. Burdiak, A. J. Harvey-Thompson, S. N. Bland, P. De Grouchy, E. Khoory, L. Pickworth, J. Skidmore, and L. Suttle, Phys. Plasmas **20**, 022705 (2013).
[19]G. F. Swadling, S. V. Lebedev, G. N. Hall, F. Suzuki-Vidal, G. Burdiak, A. J. Harvey-Thompson, S. N. Bland, P. De Grouchy, E. Khoory, L. Pickworth, J. Skidmore, and L. Suttle, Phys. Plasmas **20**, 062706 (2013).
[20]G. F. Swadling, S. V. Lebedev, A. J. Harvey-Thompson, W. Rozmus, G. C. Burdiak, L. Suttle, S. Patankar, R. A. Smith, M. Bennett, G. N. Hall, F. Suzuki-Vidal, and J. Yuan, Phys. Rev. Lett. **113**, 035003 (2014).
[21]G. F. Swadling, S. V. Lebedev, G. N. Hall, S. Patankar, N. H. Stewart, R. A. Smith, A. J. Harvey-Thompson, G. C. Burdiak, P. de Grouchy, J. Skidmore, L. Suttle, F. Suzuki-Vidal, S. N. Bland, K. H. Kwek, L. Pickworth, M. Bennett, J. D. Hare, W. Rozmus, and J. Yuan, Rev. Sci. Instrum. **85**, 11E502 (2014).
[22]P. M. Nilson, L. Willingale, M. C. Kaluza, C. Kamperidis, S. Minardi, M. S. Wei, P. Fernandes, M. Notley, S. Bandyopadhyay, M. Sherlock, R. J. Kingham, M. Tatarakis, Z. Najmudin, W. Rozmus, R. G. Evans, M. G. Haines, A. E. Dangor, and K. Krushelnick, Phys. Plasmas **15**, 092701 (2008).
[23]O. V. Gotchev, J. P. Knauer, P. Y. Chang, N. W. Jang, M. J. Shoup, D. D. Meyerhofer, and R. Betti, Rev. Sci. Instrum. **80**, 043504 (2009).

[24]D. D. Ryutov, N. L. Kugland, M. C. Levy, C. Plechaty, J. S. Ross, and H. S. Park, Phys. Plasmas **20**, 032703 (2013).
[25]V. V. Aleksandrov, V. A. Barsuk, E. V. Grabovski, A. N. Gritsuk, G. G. Zukakishvili, S. F. Medovshchikov, K. N. Mitrofanov, G. M. Oleinik, and P. V. Sasorov, Plasma Phys. Rep. **35**, 200 (2009).
[26]J. Greenly, M. Martin, I. Blesener, D. Chalenski, P. Knapp, R. McBride, B. R. Kusse, and D. A. Hammer, AIP Conf. Proc. **1088**, 53–56 (2009).
[27]S. V. Lebedev, L. Suttle, G. F. Swadling, M. Bennett, S. N. Bland, G. C. Burdiak, D. Burgess, J. P. Chittenden, A. Ciardi, A. Clemens, P. de Grouchy, G. N. Hall, J. D. Hare, N. Kalmoni, N. Niasse, S. Patankar, L. Sheng, R. A. Smith, F. Suzuki-Vidal, J. Yuan, A. Frank, E. G. Blackman, R. P. Drake, P. De Grouchy, and A. Smith, Phys. Plasmas **21**, 056305 (2014).
[28]S. V. Lebedev, F. N. Beg, S. N. Bland, J. P. Chittenden, A. E. Dangor, M. G. Haines, S. A. Pikuz, and T. A. Shelkovenko, Laser Part. Beams **19**, 355 (2001).
[29]M. Sherlock, J. P. Chittenden, S. V. Lebedev, and M. G. Haines, Phys. Plasmas **11**, 1609 (2004).
[30]D. B. Sinars, M. E. Cuneo, E. P. Yu, S. V. Lebedev, K. R. Cochrane, B. Jones, J. J. MacFarlane, T. A. Mehlhorn, J. L. Porter, and D. F. Wenger, Phys. Plasmas **13**, 042704 (2006).
[31]S. Bott, S. Lebedev, D. Ampleford, S. Bland, J. Chittenden, A. Ciardi, M. Haines, C. Jennings, M. Sherlock, G. Hall, J. Rapley, F. Beg, and J. Palmer, Phys. Rev. E **74**, 046403 (2006).
[32]G. F. Swadling, G. N. Hall, S. V. Lebedev, G. C. Burdiak, F. Suzuki-Vidal, P. de Grouchy, L. Suttle, M. Bennett, and L. Sheng, IEEE Trans. Plasma Sci. **PP**, 1 (2015).
[33]A. J. Harvey-Thompson, S. V. Lebedev, S. Patankar, S. N. Bland, G. Burdiak, J. P. Chittenden, A. Colaitis, P. De Grouchy, H. W. Doyle, G. N. Hall, E. Khoory, M. Hohenberger, L. Pickworth, F. Suzuki-Vidal, R. A. Smith, J. Skidmore, L. Suttle, and G. F. Swadling, Phys. Rev. Lett. **108**, 145002 (2012).
[34]A. J. Harvey-Thompson, S. V. Lebedev, S. Patankar, S. N. Bland, G. Burdiak, J. P. Chittenden, A. Colaitis, P. De Grouchy, G. N. Hall, E. Khoory, M. Hohenberger, L. Pickworth, F. Suzuki-Vidal, R. A. Smith, J. Skidmore, L. Suttle, and G. F. Swadling, Phys. Plasmas **19**, 056303 (2012).
[35]J. Sheffield, D. Froula, S. H. Glenzer, and N. C. Luhmann, Jr., *Plasma Scattering of Electromagnetic Radiation: Theory and Measurement Techniques*, 2nd ed. (Academic Press, 2010).
[36]S. V. Lebedev, R. Aliaga-Rossel, S. N. Bland, J. P. Chittenden, A. E. Dangor, M. G. Haines, and I. H. Mitchell, Phys. Plasmas **6**, 2016 (1999).
[37]D. Book and J. D. Huba, *NRL Plasma Formulary* (NRL, 2011).
[38]B. A. B. Trubnikov, in *Reviews of Plasma Physics*, edited by M. A. Leontovich (Consultants Bureau, New York, 1965), pp. 105–204.
[39]D. E. Post, R. V. Jensen, C. B. Tarter, W. H. Grasberger, and W. A. Lokke, At. Data Nucl. Data Tables **20**, 397 (1977).
[40]S. Braginskii, in *Reviews of Plasma Physics*, edited by M. A. Leontovich (Consultants Bureau, New York, NY, 1965), pp. 205–311.